




Magma evolution leading to porphyry Au-Cu mineralization at the Ok Tedi deposit, Papua New Guinea

Trace element geochemistry and high-precision geochronology of igneous zircon

Journal Article

Author(s):

Large, Simon J.E.; von Quadt, Albrecht; [Wotzlaw, Jörn-Frederik](#) ; [Guillong, Marcel](#) ; [Heinrich, Christoph A.](#) 

Publication date:

2018

Permanent link:

<https://doi.org/10.3929/ethz-b-000251672>

Rights / license:

[In Copyright - Non-Commercial Use Permitted](#)

Originally published in:

Economic Geology 113(1), <https://doi.org/10.5382/econgeo.2018.4543>

Funding acknowledgement:

166151 - Mineral resources: Physical dynamics driving chemical enrichment of rare metals (SNF)

This is the Green Open Access version the paper printed in *Economic Geology* (2018) 113, 39–61 (<https://doi.org/10.5382/econgeo.2018.4543>), republished together with an Electronic Appendix Large...xlsx in [researchcollection.ethz.ch](https://www.researchcollection.ethz.ch)

Magma Evolution Leading to Porphyry Au-Cu Mineralization at the Ok Tedi Deposit (Papua New Guinea): Trace Element Geochemistry and High-Precision Geochronology of Igneous Zircon

Simon J. E. Large¹, Albrecht von Quadt¹, Jörn-Frederik Wotzlaw¹, Marcel Guillong¹, Christoph A. Heinrich^{1,2}

¹Institute of Geochemistry and Petrology, ETH Zurich, 8092 Zurich, Switzerland

²Faculty of Mathematics and Natural Science, University of Zurich, CH-8006 Zurich, Switzerland

simon.large@erdw.ethz.ch

Abstract

Geological field relationships combined with spatially resolved geochemistry and high-precision U-Pb geochronology of zircons allow quantification of magmatic processes leading to porphyry emplacement and Au-Cu ore formation at Ok Tedi, the Earth's youngest giant porphyry-skarn deposit. Trace element contents in zircons were obtained by LA-ICP-MS before selected grains were removed from the sample mount, chemically abraded, spiked and dissolved for high precision U-Pb geochronology by CA-ID-TIMS. U-Pb geochronology by LA-SF-ICP-MS on abundant inherited zircon cores that occur in all intrusions together with Hf isotope analyses by solution MC-ICP-MS permitted further assessment of the degree of crustal assimilation of the upper crustal magma reservoir.

The combined chemical data and precise ages of zircons indicate closed system fractional crystallization and concurrent cooling in a common magma reservoir, from which the intrusions at Ok Tedi were successively extracted. Inherited zircon populations and Hf isotopic analyses of Pleistocene zircons record lower-crustal assimilation with Proterozoic basement. Based on CL-imaging a chemically distinct zircon population with low Th/U was identified in the youngest syn-ore intrusive rocks. These zircons indicate injection of a distinct magma into the common magma reservoir, which triggered the emplacement of the youngest porphyry, intrusion of a polymictic breccia with partly igneous matrix, and intimately associated hydrothermal Au-Cu mineralization.

Ages of chemically characterized zircon crystals extend over a total time span of 212 ± 44 kyr, recording the minimum duration of fractional crystallization in the

large magma reservoir from the time it reached zircon saturation. The youngest zircons in each intrusion resolve the emplacement of early diorite intrusions, low-grade monzodiorite porphyries, including the Sydney monzodiorite and Fubilan porphyry, into three time-resolved pulses separated by a total of ~160 kyr. The Sydney monzodiorite contains barren quartz veins and produced endoskarn and exoskarn; however, the exact timing of skarn-hosted Au-Cu mineralization is not yet clear. The emplacement of the ore-bearing Fubilan porphyry and the intrusive breccia overlap at 1.187 ± 0.022 Ma, constraining the time and duration of porphyry emplacement with associated Au-Cu mineralization. The injection of a distinct, probably more mafic magma batch into the magma reservoir preceded the emplacement of the Fubilan porphyry and the intrusive breccia by less than the resolution of 30 kyr indicating that this event was the immediate trigger for Au-Cu mineralization at Ok Tedi.

Introduction

The Ok Tedi Au-Cu deposit, located in western Papua New Guinea (Fig. 1), is one of the largest Au-Cu-rich porphyry and skarn deposits on Earth (Cooke et al., 2005) with a historic production of 4.65 Mt Cu and 14.3 Moz Au and remaining resources of 1.3 Mt Cu and 4.0 Moz Au (OTML, annual report 2016). It is also one of the youngest of its kind, with an age of ~1.4 – 1.1 Ma (Page and McDougall; 1972; van Dongen et al., 2010a).

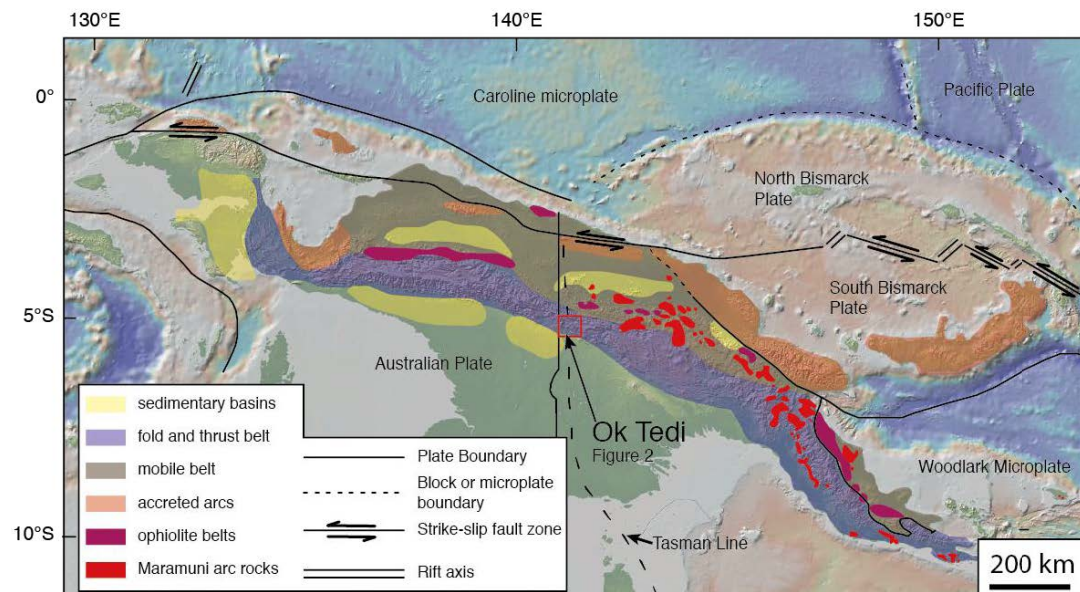


Figure 1. Geologic map of New Guinea. The four simplified tectonic units are, from south to north, the stable continental platform of the Australian craton, deformed and uplifted continental shelf rocks of the fold and thrust belt, the metamorphic and ophiolitic rocks of the mobile belt, and the accreted arcs and terranes. The suggested continuation of the Tasman line into New Guinea (e.g., Baldwin et al., 2012; Davies, 2012) separates Proterozoic basement rocks in the west from Paleozoic basement rocks in the east. The Ok Tedi deposit is located in the southern highlands of the fold and thrust belt in western Papua New Guinea. Drawn after Baldwin et al. (2012) and Hill and Hall (2003)

Magmatic-hydrothermal porphyry copper deposits are spatially associated with crystal-rich, porphyritic stocks or dikes that are emplaced into shallow crustal sedimentary and volcanic rock sequences, after extraction from deeper-seated

voluminous magma reservoirs (Sillitoe, 2010). Ore formation is believed to occur when the magma reaches H₂O-saturation and releases a metal- and sulfur-rich fluid (Sillitoe, 2010). Hydrothermal mineralization occurs almost contemporaneously with porphyritic magma emplacement, as indicated by repeated crosscutting relationships between veins and intrusions (Proffett, 2003; Seedorff and Einaudi, 2004; Redmond and Einaudi, 2010). The mechanism and timescale of fluid extraction from the larger magma reservoir is currently subject to intensive research (Candela, 1989; Huber et al., 2009; Parmigiani et al., 2016). Porphyry copper deposits are rare compared to ubiquitous, barren, silicic upper-crustal intrusions that can occur even within the same magmatic district, suggesting that unique circumstances related to the evolution of the magmatic system are required to form economic ore deposits (Sillitoe 1997, Rohrlach et al., 2005, Sillitoe and Perello 2005, Audetat et al., 2008; Wilkinson, 2013). Understanding the magmatic processes and timescales of the magma reservoirs driving porphyry ore formation is critical to broaden our understanding of these deposits and to improve exploration strategies.

Short timescales (<100 kyr to a few years) of individual pulses of hydrothermal ore formation are suggested by thermal modeling (Cathles, 1977; Weis et al., 2012) and modeling of fluid-rock equilibration by diffusion (Cathles and Shannon, 2007; Mercer et al., 2015). These studies provide physical constraints on the lifetime of a hydrothermal system in the porphyry environment. Recent high-precision zircon U-Pb geochronology studies independently confirm that short events of porphyry emplacement and hydrothermal mineralization occur at the end of a longer-term evolution of large magma reservoirs that drive ore formation (von Quadt et al., 2011; Chelle-Michou et al., 2014; Tapster et al., 2016; Buret et al., 2016, 2017). These upper-crustal reservoirs are in turn the product of the longer-term evolution of lithosphere-scale magma systems that build large volcanoes, batholiths, or camps of several large ore deposits (Sasso, 1998; Rohrlach et al., 2005; Schaltegger et al., 2009; Longo et al., 2010; Rezeau et al., 2016). With the advent of high-precision geochronology by chemical abrasion-isotope dilution-thermal ionization mass spectrometry (CA-ID-TIMS) we can now resolve the time history of protracted magma storage and crystallization in a magma chamber over several hundred thousand years, prior to the emplacement of the porphyry rocks with a time resolution of ~10 kyr. Volatiles derived from recharge by magmas of less evolved composition may trigger fluid saturation and porphyry emplacement (Buret et al., 2016; Tapster et al., 2016; Buret et al., 2017). The importance of mafic magma injection into highly crystalline and silicic magma reservoirs as a trigger for porphyry mineralization has first been inferred from mingling textures (Hattori and Keith, 2001) and melt inclusion studies (Halter et al., 2005).

Field exposures at economic porphyry deposits are typically restricted to the top portion of these transcrustal magmatic-hydrothermal systems. Relationships between porphyry deposits and upper-crustal magma chambers are known from a few tectonically tilted deposits (e.g., Yerington: Dilles, 1987) and geophysical models (Steinberger et al., 2013). In contrast to barren intrusions, investigations of porphyry deposit-related magmas based on whole-rock and major mineral chemistry are hampered by the thermal and chemical overprint associated with hydrothermal alteration. Zircon is a refractory mineral that remains, once grown, practically unaffected by later magma evolution and hydrothermal alteration of

the rock (Cherniak and Watson, 2003). Preferential incorporation of diagnostic trace elements in the zircon lattice and the possibility of high-precision U-Pb dating of zircon growth (Chiaradia et al., 2013), make these accessory crystals a powerful tracer for the evolution of upper crustal magma reservoirs in porphyry environments.

We obtained *in situ* trace-element analyses of zircons by laser ablation-inductively coupled plasma-mass spectrometry (LA-ICP-MS), subsequently extracted selected crystals from the grain mount for chemical abrasion, and finally dated each of the cleaned crystals by ID-TIMS to obtain a high-precision U-Pb age. Applying these techniques to zircons from the very young intrusive suite of the Ok Tedi deposit allows unprecedented precision in resolving the timescales of magma evolution, incremental porphyry emplacement and porphyry Au-Cu mineralization.

Geological Background

Regional geology and tectonic framework

The Ok Tedi intrusive complex is located in the center of the island of New Guinea, in the Western Province of Papua New Guinea, about 15 km east of the border with the West Papua province, Indonesia. The Ok Tedi mine is situated at an elevation of about 2000 m above sea level in the southern highlands of the fold and thrust belt that is part of the New Guinea orogen.

Geologically, New Guinea can be subdivided into four simplified tectonic regions from south to north (Fig. 1; Hill and Hall, 2003; Davies, 2012; Holm et al., 2015): (1) the stable platform in southern New Guinea with sedimentary basins on Australian continental basement, (2) the deformed and uplifted lithologies of the former Australian passive margin known as the fold and thrust belt, (3) the metamorphic rocks and ophiolites in the mobile belt and (4) the northern accreted arcs and terranes.

The tectonic evolution of New Guinea is very complex with several terrane collision and accretion events that, together with the folding and uplift of the northern margin of the Australian Plate, formed the alpine New Guinea orogen, arc magmatism, debated subduction dynamics and underlying inherited crustal architecture of the Australian Plate (e.g. Hill and Hall, 2003; Cloos et al., 2005; Baldwin et al., 2012; Davies, 2012; Holm et al., 2015). Geologically, New Guinea is part of the northern margin of the Australian continent that has been exposed to a collisional environment since the Miocene (Hill and Hall, 2003; Baldwin et al., 2012; Davies, 2012). The collision resulted in the formation of the New Guinea orogen and the complex plate boundary zone observed today, including ophiolites and several accreted arcs (Johnson and Molnar, 1972; Gaina et al., 2007).

The current style of New Guinea's northern plate boundary is still debated with north- and south-dipping subduction being suggested (Tregoning and Gorbato, 2004; Cloos et al., 2005 and Baldwin et al., 2012). Ok Tedi is part of an intermediate composition volcanic and intrusive rock suite emplaced in the New Guinea orogen during the Late Miocene to Pliocene (Page, 1976; Hill and Hall, 2003; Cloos et al., 2005). Volumetrically, these magmatic rocks are minor but host many of New Guinea's mineral deposits, including the Frieda River prospect as well as the Porgera (~6 Ma; Richards et al., 1990), Grasberg (~3 Ma; Pollard et al.,

2005), and Ok Tedi (~1.3 Ma; Rush and Seegers, 1990) mines. Several authors suggest partial melting of the lower crust following arc-continental collision and crustal thickening as the triggers for the Miocene magmatic activity (Johnson et al., 1978; Johnson and Jaques, 1980). Whereas, Cloos et al. (2005) and Holm et al. (2015) suggest that the generation of magmas was linked to the delamination of northward subducting lithosphere, which led to decompression of thinned crust, and asthenospheric upwelling.

District geology

The Ok Tedi intrusive complex is located in the Star Mountains copper province of the fold and thrust belt (Fig. 2). The Star Mountains host a number of regional intrusive centers, some of which are associated with varying amounts of Au-Cu mineralization (Arnold and Griffin, 1978). A group of magmatic rocks, including the Ok Tedi complex, the Anju andesite and the Mt. Ian complex, are roughly aligned on a north-northeast trend possibly following an older basement structure (Fig. 2; Arnold and Griffin, 1978). The magmatic rocks of the Star Mountains intruded into the folded sedimentary rocks within the western extension of the Muller anticline (Fig. 2), a northwest trending feature of the fold and thrust belt. The majority of intrusive rocks occur as subvolcanic stocks, except for the large Antares complex, which is suggested to represent an exposed batholith (Page, 1975; Arnold and Griffin, 1978). Most of these intrusions are calc-alkaline in composition (Arnold and Griffin, 1978). Emplacement ages vary between ~7 Ma and ~1 Ma with only the younger intrusions (<4.5 Ma) being associated with Au-Cu mineralization (Page, 1975).

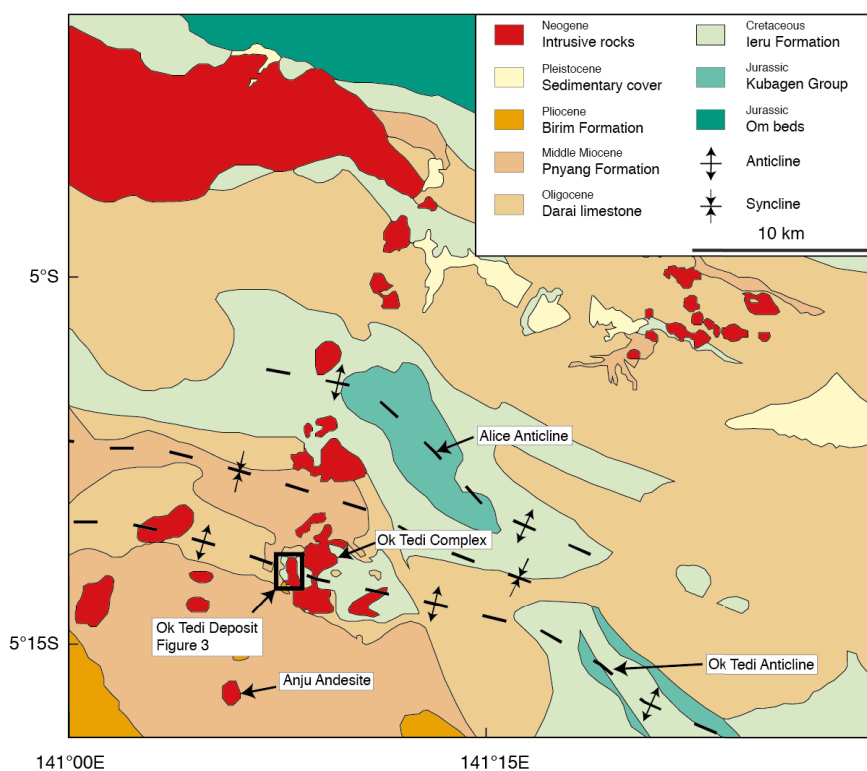


Figure 2. Regional geologic map of the Star Mountains in western Papua New Guinea. The Ok Tedi deposit is hosted within the Ok Tedi intrusive complex. The Anju Andesite intrusion is located ~10 km southwest of Ok Tedi. The Ok Tedi Anticline and Alice Anticline are western splays of the Muller Anticline. Redrawn after Arnold and Griffin (1978) and Mason (1997).

Deposit geology

The Ok Tedi porphyry-skarn Au-Cu deposit located in the western part of the Ok Tedi intrusive complex (Fig. 2) is the main focus of this study. Mineralization is characterized by disseminated and vein-hosted sulfides in the main Fubilan monzonite porphyry, high-grade magnetite-sulfide skarns and sulfide-rich igneous to hydrothermal breccias. The Ok Tedi complex intruded a sedimentary sequence consisting of basal Cretaceous Ieru siltstones and sandstones that are unconformably overlain by Oligocene Darai limestone, which in turn, is overlain by mudstones and siltstones of the Miocene Pnyang Formation. Each of these units can reach thicknesses of >1 km (Pigram et al., 1989). The Ok Tedi deposit is closely associated with two north-dipping faults, the Parrots Beak thrust and the Taranaki thrust (Fig. 3). Both faults are suggested to have caused a vertical repetition of Darai limestone and Ieru siltstone and to have experienced pre- and post-mineralization movement (Mason, 1997; Van Dongen et al., 2013).

Previous studies have not yet established a widely accepted model for the intrusive geology at the Ok Tedi deposit. Different numbers of distinct intrusions are described in the literature (Bamford, 1972; Rush and Seegers, 1990; Doucette, 2000; Van Dongen et al., 2010a, 2010b; Pollard, 2014). The current mine geology office distinguishes between the Fubilan monzonite porphyry and the Sydney monzodiorite, but older mine maps also show a third intrusive phase that we term biotite monzodiorite (Fig. 3). The Fubilan monzonite porphyry is a near cylindrical vertical stock and is considered to have intruded both monzodiorites (Bamford, 1972). A characteristic core of intense quartz stockwork veining but low Au-Cu grade is located in the center of the Fubilan monzonite porphyry (Fig. 3).

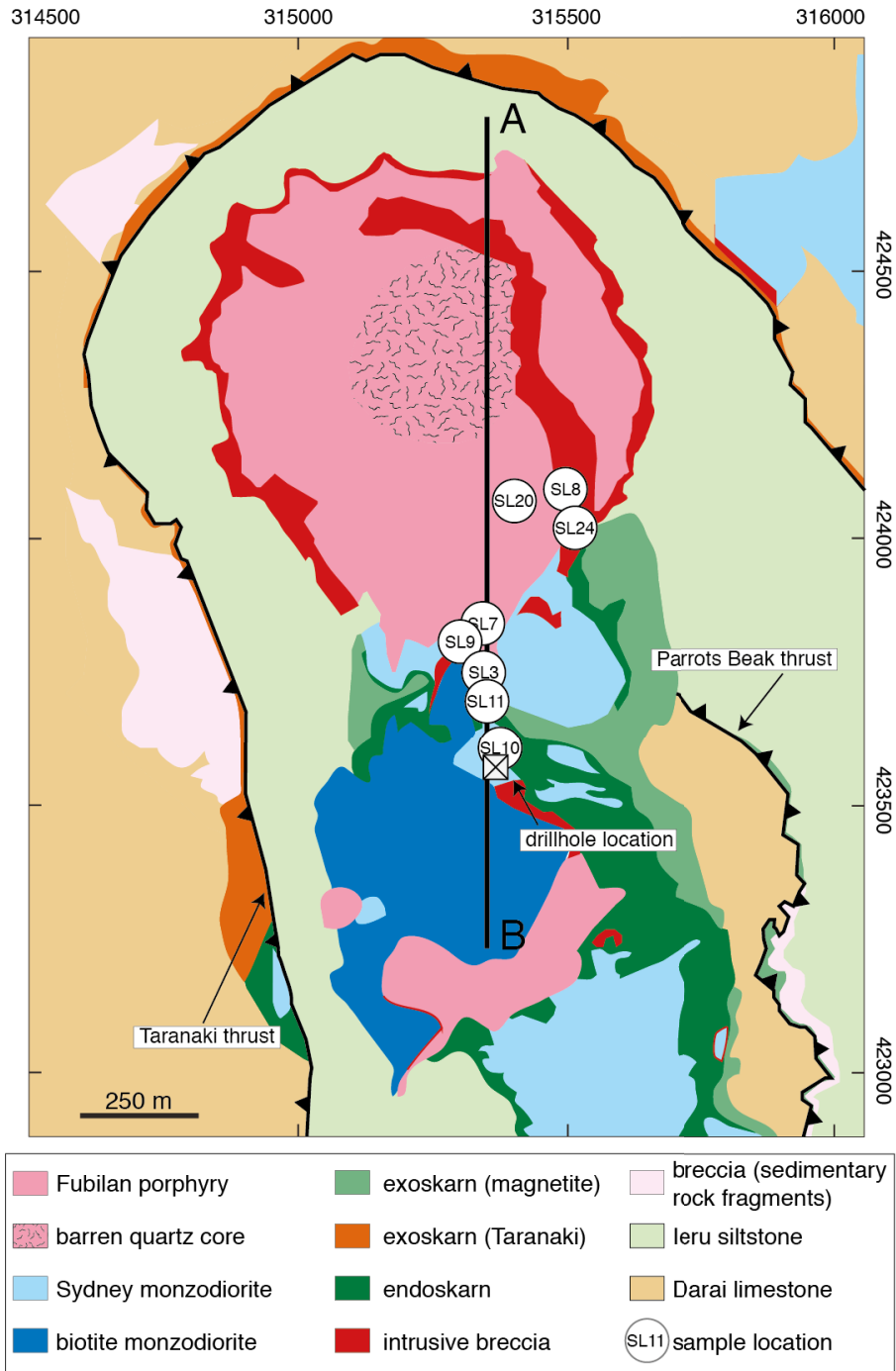


Figure 3. Geologic map of the Ok Tedi porphyry-skarn Au-Cu deposit. The Sydney and biotite monzodiorite and the later Fubilan porphyry intruded into the surrounding sedimentary sequence. Breccias occur throughout the deposit but the intrusive breccias containing high Au-Cu ore grade are concentrated in the intrusive stocks and their immediate surroundings. The crossed square indicates the collar of the deep drillhole in Fig. 4 (section A-B). Sample locations are approximate (for exact coordinates consult the Appendix. Map is based on mine maps from Ok Tedi Mining Limited, Pollard (2014) and own observations.

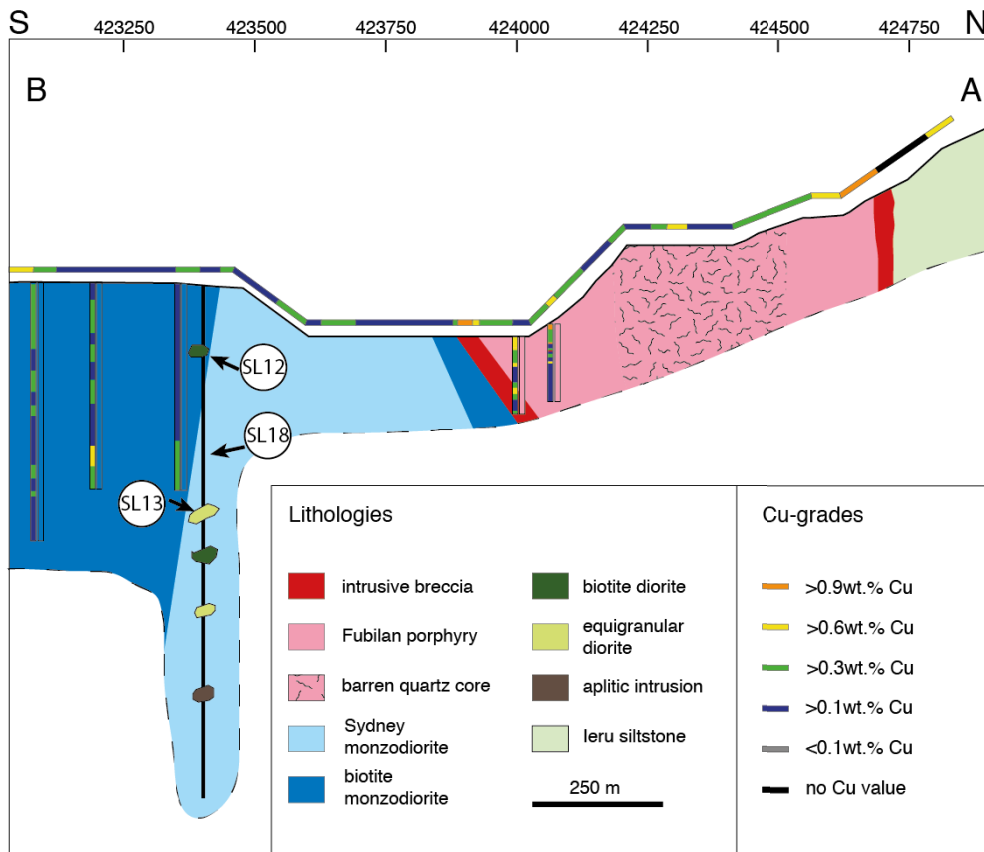


Figure 4. North – south cross-section through the Ok Tedi deposit based on field observations and drillhole data through the southern part of the pit (A-B in Fig. 3). The Fubilan porphyry and the breccias intrude into the monzodiorites and sedimentary rocks. Ore grades indicate enrichment of Cu in the intrusive breccia. Selected exploration drillholes are displayed with Cu grades. The deep drillhole intersected an aplitic intrusion, a biotite diorite and an equigranular diorite, mainly in the deeper parts.

We identified three main intrusions within the pit and a further three in a deep drillhole that was recently drilled just south of the Fubilan monzonite porphyry (see Fig. 3 and 4 for the drillhole location). The main intrusion at the center of the deposit is the Fubilan monzonite porphyry, hereafter only referred to as the Fubilan porphyry (Fig. 5C). It is mainly composed of plagioclase and K-feldspar phenocrysts (<1 cm in diameter) in a groundmass of quartz, alkali feldspar and biotite (Fig. 6A, 6B). K-feldspar occurs as a primary mineral but also replaces plagioclase as a result of pervasive potassic alteration. Accessory phases include apatite, zircon, magnetite and titanite. The latter is partly replaced by an opaque phase, most likely ilmenite (Fig. 7A). Biotite is the only mafic phase still present in this intrusion and occurs both as primary phenocrysts and as secondary replacement minerals. Primary hornblende has been replaced by hydrothermal biotite ± sulfides (Fig. 7B). The Fubilan porphyry contains abundant disseminated and vein-hosted chalcopyrite and pyrite.

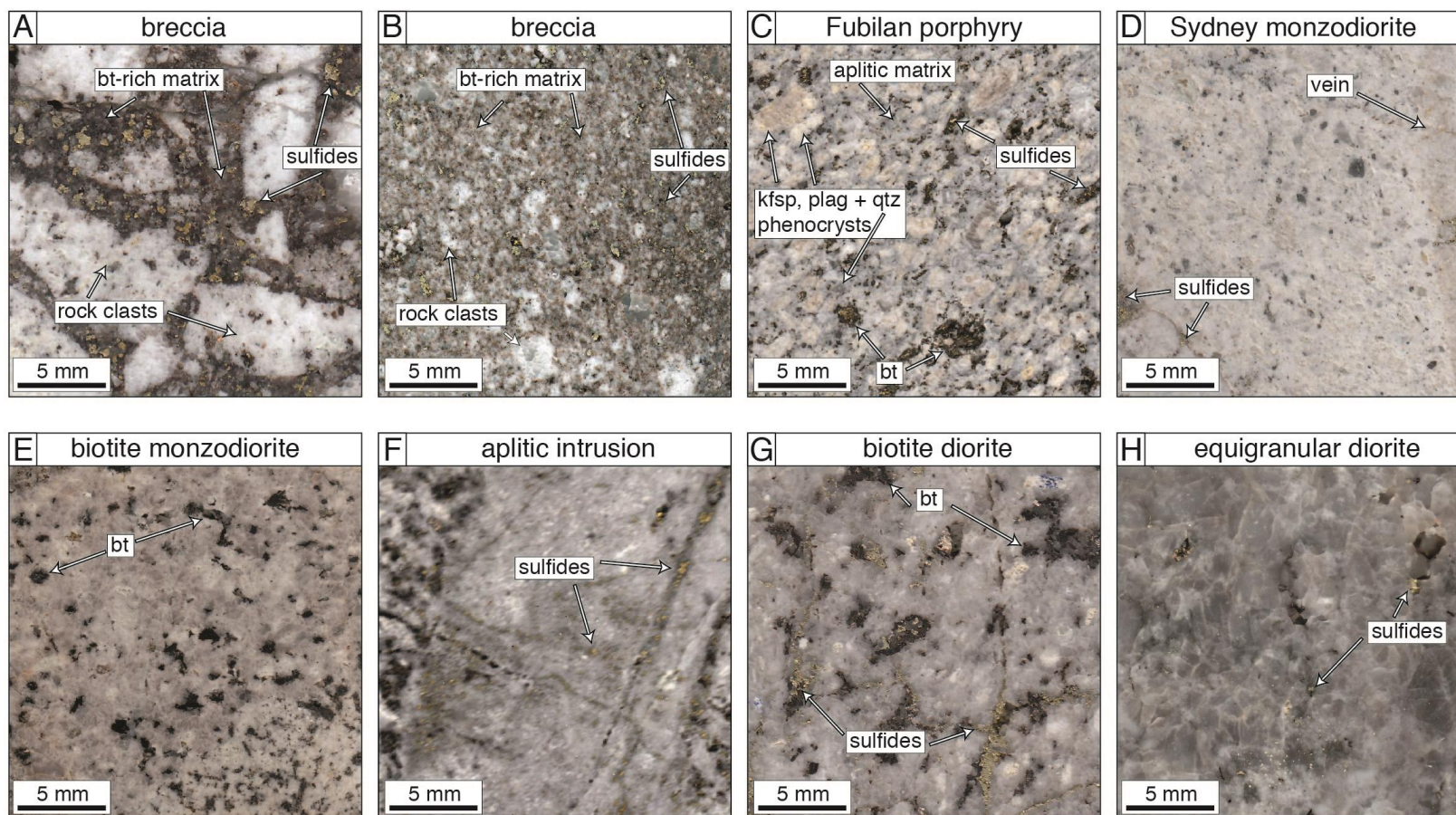


Figure 5. Slab photos of rock types at the Ok Tedi deposit. **A, B:** Sulfide-rich breccias range from clast dominated and biotite-rich (A) to matrix dominated (B). **C:** The Fubilan porphyry contains plagioclase and alkali feldspar phenocrysts generally <1 cm and biotite flakes that form larger aggregates intergrown with chalcopyrite and pyrite. **D:** The Sydney monzodiorite is fine-grained and equigranular to sub-porphyritic. **E:** The biotite monzodiorite is equigranular and fine-grained (<1 mm) and contains characteristic large biotites >1 mm. **F-H:** The aplitic intrusion (F), biotite diorite (G) and equigranular diorite (H) are all dominated by quartz, plagioclase and alkali feldspar; these intrusions appear to pre-date the Au-Cu mineralization event, as they have been crosscut by quartz-sulfide veins. The biotite and equigranular diorites have grain sizes <1 cm and the biotite diorite contains characteristic biotites up to 5 mm. Abbreviations: bt = biotite, kfsp = alkali feldspar, plag = plagioclase, qtz = quartz.

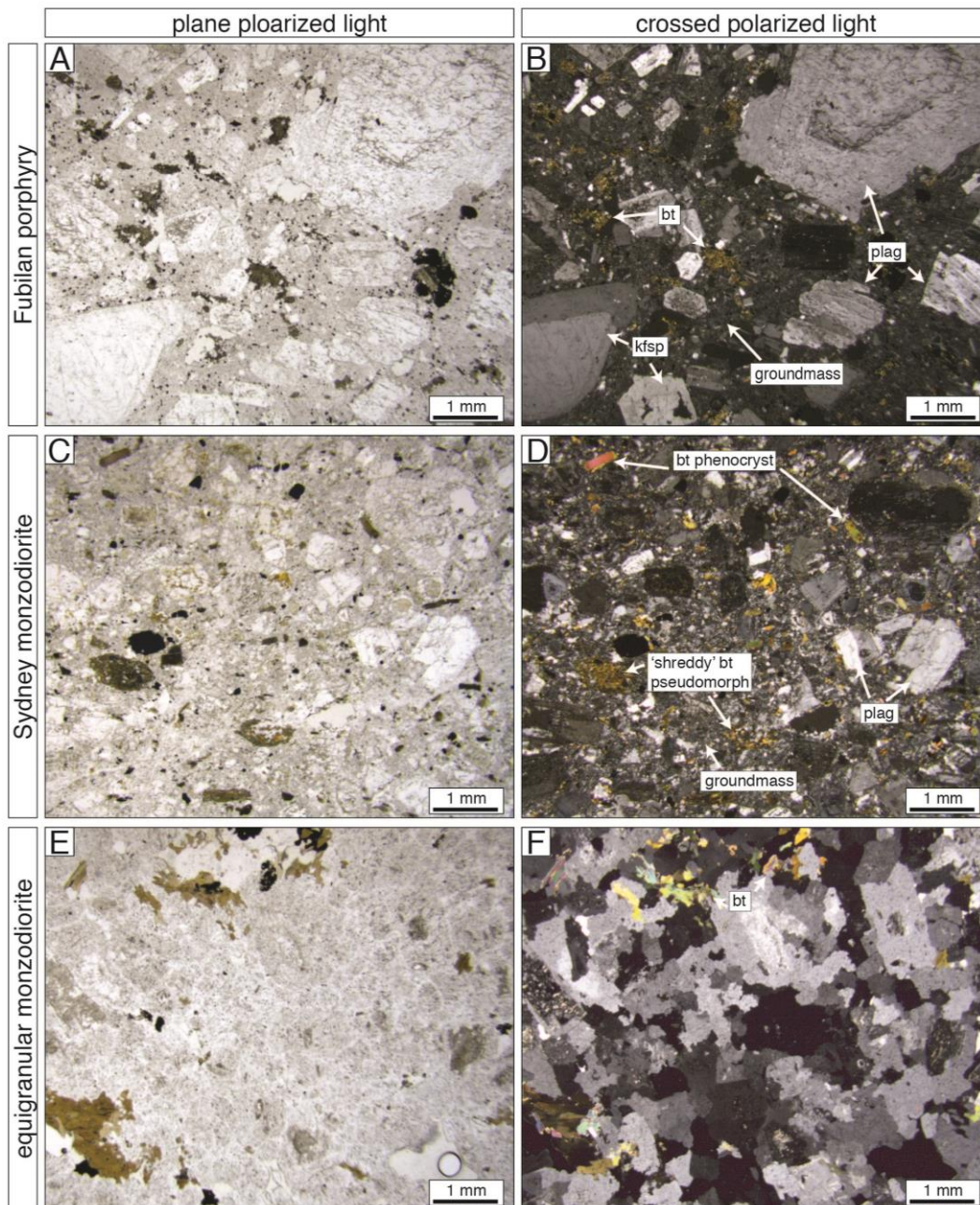


Figure 6. Thin section images of main intrusive units in plain polarized (left) and crossed polarized light (right). **A, B:** The Fubilan porphyry is characterized by plagioclase and alkali-feldspar phenocrysts in a groundmass of feldspar, quartz and biotite. The majority of fine grained biotite is secondary. **C, D:** The subporphyritic Sydney monzodiorite contains plagioclase phenocrysts (<1 mm) and biotite phenocrysts (<500 μm) in a fine-grained groundmass containing quartz, feldspar and fine-grained hydrothermal biotite. **E, F:** The equigranular biotite monzodiorite has equigranular quartz and feldspar crystals (<1 mm) and contains characteristic aggregates of biotite flakes. Abbreviations: fsp = feldspar, bt = biotite, plag = plagioclase, kfsp = alkali feldspar.

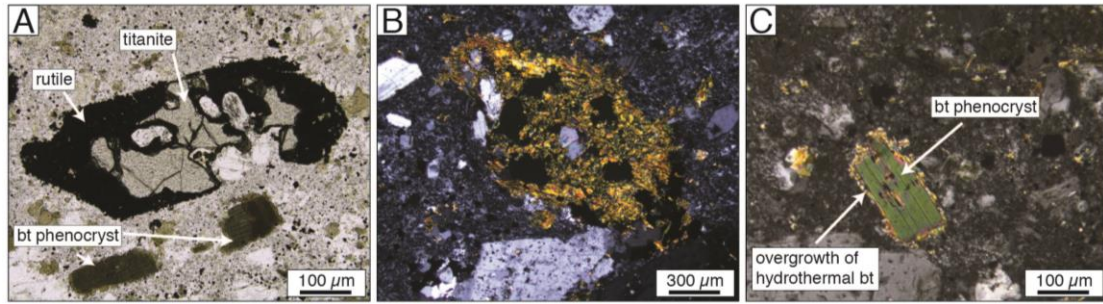


Figure 7. Thin section images in plane polarized light (A, B) and crossed polarized light (C) of different minerals or replaced minerals within the Ok Tedi deposit. A: Titanite replaced by ilmenite and other secondary minerals in highly altered Sydney monzodiorite. B: Secondary biotite and minor sulfides replacing primary amphibole in the Fubilan porphyry. C: Primary biotite overgrown by fine-grained secondary biotite associated with potassic alteration.

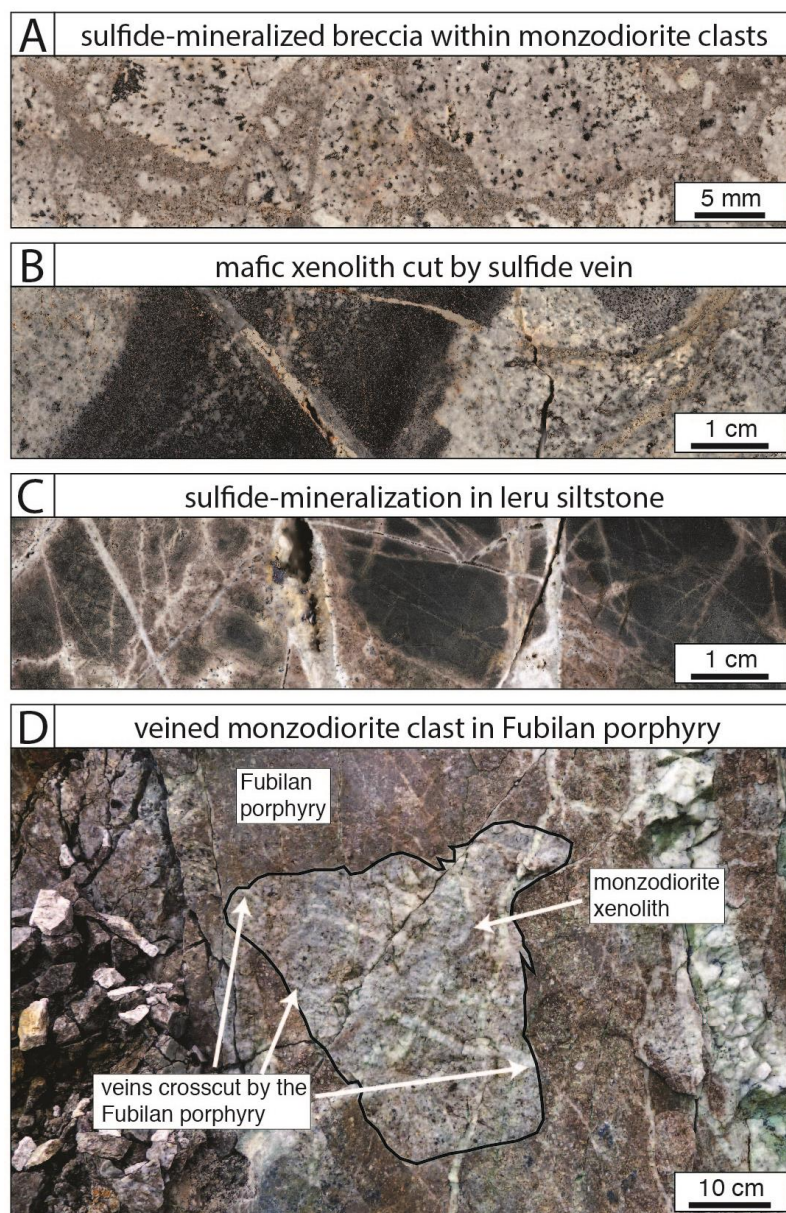


Figure 8. Selected rock relationships observed in the Ok Tedi deposit. A: Breccia with a quartz-biotite-cemented sandy matrix crosscutting the biotite monzodiorite. B: Mafic xenolith cut by a quartz-sulfide vein. C: Thick quartz-molybdenite-chalcopyrite veins (<1 cm) with a potassic alteration halo crosscutting the Ieru siltstone. D: Monzodiorite xenolith with truncated veins within Fubilan porphyry.

The Sydney monzodiorite and biotite monzodiorite mainly occur in the southern part of the deposit. Xenoliths of both monzodiorites that contain truncated veins occur in the Fubilan porphyry (Fig. 8D), suggesting that emplacement of both monzodiorites and mainly barren hydrothermal activity occurred before emplacement of the Fubilan porphyry. The Sydney monzodiorite is fine-grained and equigranular to slightly porphyritic (Fig. 5D). It contains plagioclase, alkali feldspar, minor quartz, primary biotite and abundant secondary biotite (Fig. 6C, 6D). Secondary biotite locally overgrows primary biotite (Fig. 7C). Samples with subtle to weak alteration display primary clinopyroxene and hornblende (cf. Bamford, 1972; van Dongen et al., 2010b); whereas, these minerals are replaced by secondary biotite in more altered samples. Accessory phases include titanite, zircon, apatite and magnetite. The biotite monzodiorite (Fig. 5E) is similar in its mineralogy to the Sydney monzodiorite, but is equigranular and generally coarser grained. It contains characteristic igneous biotite that forms aggregates up to a few mm across (Fig. 6E, 6F). Both monzodiorites can contain significant amounts of pyrite and chalcopyrite but generally contain less than the Fubilan porphyry. Whole-rock analyses by van Dongen et al. (2010b) of least-altered samples of the Fubilan porphyry and the Sydney monzodiorites indicate high alkali and low iron and magnesium contents, classifying these rocks as shoshonites. However, this classification should be treated with caution as even slight potassic alteration can result in a high-K composition.

Intrusive, igneous to hydrothermal breccias (Fig. 5A, 5B, 8, 9) occur throughout the deposit, mainly bordering the three main intrusions and particularly in and around the Fubilan porphyry (Fig. 3). We focus on intrusive breccias associated with the Fubilan porphyry that contain diverse magmatic rock clasts, with or without clasts of sedimentary rocks, and commonly containing a juvenile igneous component. We call them intrusive breccias, because their polymictic nature demonstrates significant clast transport during emplacement, irrespective of their variable matrix. By contrast, breccias in sedimentary rocks are mainly composed of local sedimentary clasts (Fig. 3), and these breccias were not sampled in this study. Bamford (1972), Arnold and Fitzgerald (1977), Davies et al. (1978), van Dongen et al. (2013) and other authors described the breccias at Ok Tedi as magmatic-hydrothermal, recognizing their significance for high-grade Cu-Au mineralization (Pollard, 2014). Similar transitional igneous to hydrothermal breccias are known from other porphyry deposits (e.g., Sillitoe, 1985; Landtwing et al., 2002). The intrusive breccias at Ok Tedi span a continuous range in textures from a polymictic mixture of clasts in a dominantly felsic igneous matrix with partly broken plagioclase phenocrysts (Fig. 9A), through sandy clast-supported breccias with a likely juvenile ash component cemented by hydrothermal biotite, K-feldspar and quartz (Fig. 9B, C), to purely hydrothermal breccias with angular clasts that are cemented by fluid-precipitated biotite, Cu-Fe-sulfides and quartz leaving ample open vug space (Fig. 9D). The entire spectrum of igneous to hydrothermal breccias is characterized by abundant red-brown hydrothermal biotite and pervasive potassic alteration of plagioclase to K-feldspar. Their biotite content, especially in the well-mixed sandy variety, is distinctly higher than in all potassically altered porphyries and monzodiorites, giving them an overall more mafic appearance. The intrusive breccias sampled for our geochronology study contain: (1) angular clasts of monzodiorite and Fubilan porphyry with truncated earlier veins; (2) irregular rounded and sharply bounded (Fig. 9A upper right) or

partially disintegrated (9A center) blobs of biotite-rich material with partly broken feldspar phenocrysts, secondary biotite and disseminated Cu-Fe-sulfide (Fig. 10C, 10D), interpreted as biotite-altered mafic igneous enclaves or as partly-cemented clasts of biotite-rich sandy breccia; and (3) felsic material in which juvenile clasts are commonly hard to distinguish and delineate from the igneous-textured felsic matrix of the breccia (Fig. 9A). Veined Fubilan porphyry xenoliths contain partly sericitized plagioclase phenocrysts, whereas plagioclase in the igneous breccia matrix is directly replaced by K-feldspar only (Fig. 10A, 10B), both features showing that the intrusive breccia contains juvenile material that slightly postdates the Fubilan porphyry. On the other hand, the textural similarity between Fubilan groundmass and the igneous breccia matrix (Fig. 10A, 10B), and the intrusive emplacement of breccias in and along the Fubilan contact indicate that the Fubilan magma and the juvenile igneous component of the breccias are closely related, and that the Fubilan porphyry and the breccias jointly contributed to hydrothermal Cu-Au mineralization. In contrast to many other porphyry Cu deposits (e.g. Gustafson and Hunt, 1975; Sillitoe, 2010), Ok Tedi contains no post-ore porphyry intrusion that crosscuts the mineralized skarns or breccias, suggesting that the breccias are the youngest feature in the magmatic history of the deposit. However, at least one fluid pulse post-dates breccia emplacement as evidenced by molybdenite-bearing veins crosscutting the intrusive breccia.

Three additional igneous lithologies were identified in a deep drillhole (Fig. 3, 4): an aplitic intrusion (Fig. 5F), a biotite diorite (Fig. 5G) and an equigranular diorite (Fig. 5H). Based on geometric relationships in core we could not distinguish whether they are dikes or xenoliths within the monzodiorite; however, based on geochronological data shown later, these intrusive phases are likely xenoliths. The aplitic intrusion has grain sizes $<50\ \mu\text{m}$, is equigranular and contains predominantly plagioclase and minor quartz (Fig. 5F). The biotite diorite and equigranular diorite are coarse-grained with grain sizes $<1\ \text{cm}$ in diameter. Their composition is dominated by plagioclase and biotite aggregates (Fig. 5G, 5H). They exhibit characteristic large cm-sized vugs. The biotite diorite is characterized by biotite and biotite aggregates up to a few centimeters in size (Fig. 5G).

The largest fraction of Cu and Au at Ok Tedi is hosted in disseminated and vein-hosted porphyry-style sulfide mineralization, in skarn mineralization or within sulfides of the intrusive breccias. A gold-enriched cap that resulted from supergene leaching and redeposition, above the Fubilan porphyry has been mined out (Rush and Seegers, 1990). Metal-grades vary strongly depending on mineralization type but disseminated porphyry-style mineralization occurs in all intrusive rocks outcropping in the pit. Ore grades in the Fubilan porphyry can be economic ($\sim 0.5\ \text{wt. \% Cu-equivalent}$) whereas grades within the monzodiorites are mainly sub-economic ($<0.3\ \text{wt. \% Cu-equivalent}$). The intrusive breccias commonly have elevated metal concentrations compared to the porphyry-style mineralization ($>0.5\ \text{wt. \% Cu-equivalent}$; Fig. 4). Van Dongen et al. (2013) distinguish two different skarn-replacement mineralization types, the Taranaki massive pyrite type that occurs along the Taranaki thrust and the high-grade magnetite skarn type ($1\ \text{wt. \%} - 2.5\ \text{wt. \% Cu-equivalent}$) that occurs mainly at the contacts of the monzodiorites with the Darai limestone (cf. Fig. 3). Additionally, vein-style mineralization in the sedimentary rocks surrounding the intrusive stocks is characterized by K-feldspar, biotite, quartz, pyrite, chalcopyrite \pm molybdenite and associated potassic alteration (Fig. 8D).

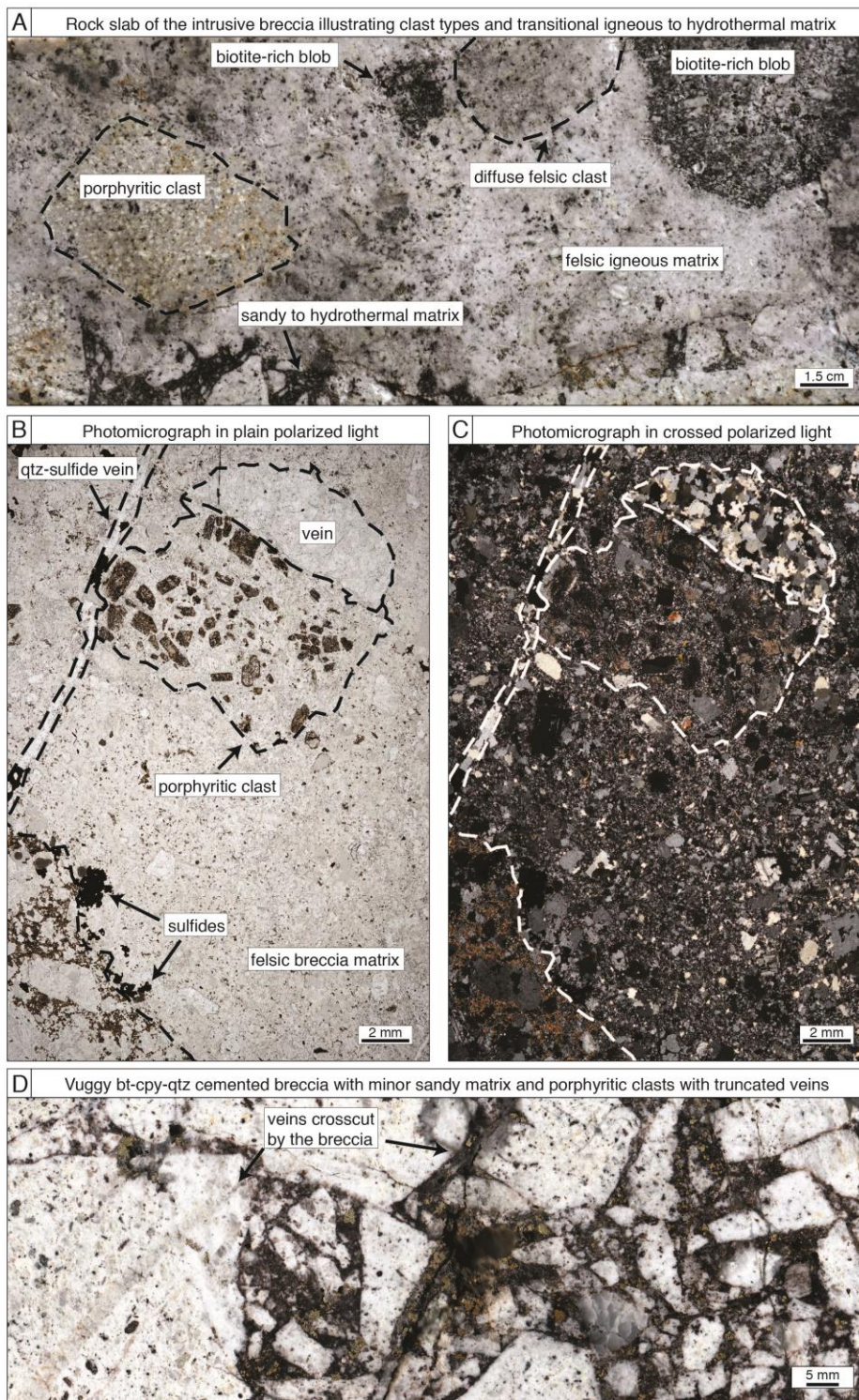


Figure 9. Photographs (A, D) and photomicrographs (B, C) of intrusive breccias at the contact of the Fubilan porphyry and the biotite monzodiorite. **A:** Breccia with dominantly igneous matrix grading into sandy-hydrothermal matrix (lower left corner). The breccia contains porphyritic clasts of the Fubilan porphyry, diffuse felsic clasts resembling the igneous matrix, and variably digested biotite rich blobs that may indicate magma mingling (mafic enclaves) or clast incorporation in a transitional igneous to sandy matrix. **B, C:** Photomicrographs in plain and crossed polarized light of a section from the breccia: Porphyritic clasts and vein fragments entrained in the igneous intrusive breccia. Sulfides occur at the contact of the igneous intrusive breccia to the biotite-rich blob. Quartz-sulfide vein crosscutting the igneous breccia. Sericitized plagioclase only occurs in the porphyritic clast but not in the breccias. **D:** Clast-dominated hydrothermal endmember of the intrusive breccia at the contact of the Fubilan porphyry with the biotite monzodiorite. Angular clasts are cemented by biotite, abundant Cu-Fe-sulfides and quartz, with open vug space. Abbreviations: bt = biotite, cpy = chalcopyrite, qtz = quartz.

The timing of extensive skarn mineralization at Ok Tedi is difficult to constrain from geologic relationships, notably regarding the skarns associated with the Taranaki thrust that have no contacts with the stockwork-veined porphyries. Clasts of magnetite skarn ore occur within the intrusive breccia (cf. Arnold and Griffin, 1978; Pollard, 2014) and a piece of mineralized magnetite skarn was identified within the Fubilan porphyry. However, it is not clear whether a limestone xenolith was selectively mineralized *in situ* during Fubilan porphyry-related veining, or whether previously mineralized magnetite skarn was incorporated as a xenolith into the Fubilan magma. Pollard et al. (2015) reported Re-Os dates on molybdenite ranging from 1.32 to 1.13 Ma, but no correlation with geological crosscutting relationships and Au-Cu mineralization are known so far.

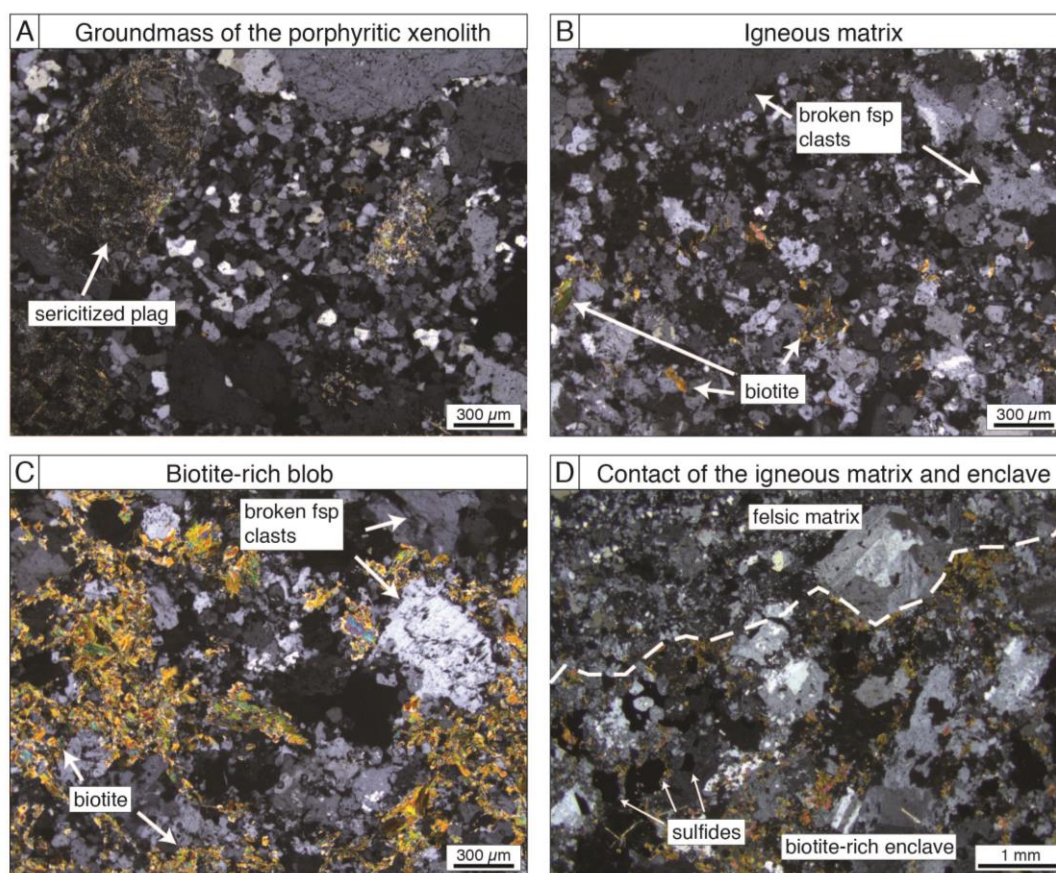


Figure 10. Photomicrographs in crossed polarized light. **A:** Groundmass of the porphyritic clast in Fig. 9B, 9C. **B:** Matrix of the igneous intrusive breccia with grainsizes similar to the groundmass in (A). **C:** Matrix of the biotite-rich blob. **D:** Contact of the igneous intrusive breccia with the biotite-rich blob. Most sulfides are within the biotite-rich blob or at the contact. All dark black patches are sulfides. Abbreviations: qtz = quartz, plg = plagioclase, fsp = feldspar.

Materials and Analytical Methods

Following three weeks of core logging and outcrop mapping with company geologists in the open pit in May 2014, we selected three samples of the intrusive breccia (SL8, SL9, SL24), two samples of the Fubilan porphyry (SL7, SL20), two samples each from the Sydney (SL10, SL11) and biotite monzodiorite (SL3, SL18) and one sample each from the equigranular diorite (SL13), biotite diorite (SL12) as well as the andesitic Anju intrusion (Fig. 3 and 4 for sample locations). The following procedure allowed spatially resolved trace element analysis that

tracked the chemical evolution of the magma from which the zircon crystallized in combination with high precision U-Pb geochronology to place the geochemical record of individual zircon crystals into a precise temporal context. Separated zircon populations were first imaged using scanning electron microscopy cathodoluminescence (CL) before *in situ* Laser Ablation analysis for trace elements and U-Pb isotopes using a sensitive sector-field ICP-MS. Low-precision but spatially resolved LA-ICP-MS U-Pb ages were used for evaluating inherited zircon populations represented by significantly older cores and to select inheritance-free zircons for subsequent dissolution and analysis by ID-TIMS. In a second step, selected crystals were removed from the epoxy mount and analyzed employing CA-ID-TIMS to obtain high-precision U-Pb ages. Selected CA-ID-TIMS dated crystals were also analyzed for Hf isotope ratios by solution nebulization multi collector (MC)-ICP-MS.

Sample preparation

Rocks were cut into small pieces, and in the case of the breccia sample (SL8, SL9, SL24), clasts of Fubilan porphyry and earlier monzodiorite were removed as far as possible. Selected pieces were subsequently disintegrated by high-voltage pulses in a Selfrag Lab™ at ETH Zurich. Heavy and light mineral fractions were separated by panning and subsequently by density separation using methylene iodide (3.3 g/cm³). Magnetic separation with a Frantz isodynamic separator was used for large heavy mineral aliquots. Hand picked zircons were annealed at 900°C in quartz crucibles for 48 hours prior to mounting them in epoxy resin. Grain mounts were ground and polished to expose crystal interiors. Polished grain mounts were then carbon coated and zircons were imaged using a Tescan EOscan VEGA XL Series 4 Scanning Electron Microscope (SEM) in cathodoluminescence (CL) and back-scattered electron mode at the Department of Materials, ETH Zurich.

In situ LA-ICP-MS trace element and U-Pb analysis

Spots of 20 or 30 µm diameter within the zircons were selected based on the SEM-CL images. Generally one spot was chosen in the interior (core) and one for the exterior (rim) part of the zircon with further spots selected after individual evaluation of the CL image. *In situ* trace element analyses and U-Pb geochronology were conducted by LA-ICP-MS at the Institute of Geochemistry and Petrology, ETH Zurich using a 193 nm Resolution (S155) ArF excimer laser coupled to a Element SF ICPMS (see supplementary Material for metadata and further details). The output energy was typically ca. 2 J/cm² and a 5 Hz pulse repetition rate was used. The ablation was under helium flow of 0.7 L/min. Argon was admixed to the aerosol within the funnel of the ablation cell to transport the ablated material to the ICP for ionization. Dwell times range from 5 – 30 ms and peak hopping was employed. Oxide generation was optimized at ThO⁺/Th⁺ = <0.3%. For each analysis a baseline was measured for 25 seconds followed by 40 seconds of ablation. Elemental concentrations were calculated using the IGOR based Iolite software (Paton et al., 2011). The stoichiometric Si concentration of 15.2 wt.% for zircon

was used as an internal standard. NIST 610 glass was used as the primary external trace element standard and was measured twice each 25 zircon analyses.

For U-Pb geochronology the masses 202, 204, 206, 207, 208, 232, 235 and 238 were measured. Total ablation time was set to 30 seconds with a gas blank/background measurement of 10s. Age data were collected in runs of 30 samples bracketed before and after by three analyses of the primary reference material GJ-1 (Jackson et al., 2004) and secondary reference zircons 91500 (Wiedenbeck et al., 1995), Temora (Black et al., 2003) and AusZ7.5 (von Quadt et al., 2016). Data reduction was performed with the IGOR based Iolite v2.5 (Paton et al., 2011) and Vizual Age (Petrus and Kamber, 2012) software. Obtained isotope ratios and dates are corrected for mass bias, instrumental drift and downhole fractionation using primary reference material.

In this publication we present ages obtained by LA-ICP-MS <1 Ga by their $^{206}\text{Pb}/^{238}\text{U}$ age and ages >1 Ga by their $^{207}\text{Pb}/^{206}\text{Pb}$ age. Furthermore, spot analyses that encountered Proterozoic and Pleistocene age domains in a single ablation can be qualitatively interpreted using the $^{207}\text{Pb}/^{206}\text{Pb}$ age as the ^{206}Pb and ^{207}Pb component of the Pleistocene material is very minor compared to the Pb derived by U-decay since Proterozoic times.

Analyzed ages and trace elements of spots with elevated Al, P, Ca, Mn or Fe were discarded as these values indicate the presence of mineral (e.g., apatite or feldspar) or melt inclusions.

CA-ID-TIMS

High-precision U-Pb ages were obtained from a total of 67 zircons (59 previously analyzed by LA-ICP-MS) employing ID-TIMS at the Institute of Geochemistry and Petrology of ETH Zurich using procedures outlined in von Quadt et al. (2016). All zircons were pre-treated using chemical abrasion (CA) techniques modified from Mattinson (2005) although post-crystallization Pb-loss is likely to be insignificant in these young and low-U zircons. For CA pre-treatment, selected annealed zircons were placed into 3 ml Savillex beakers, rinsed with 4 N HNO_3 and subsequently transferred into 200 μl Savillex micro-capsules with 80 μl concentrated HF + trace HNO_3 , placed in a high pressure Parr bomb and chemically abraded for 12 – 15 hours at 180°C. Chemically abraded zircons were transferred back into their 3 ml Savillex beakers, fluxed for 12 hours in 6 N HCl at ~85°C and ultrasonically cleaned in ultrapure H_2O and 4N HNO_3 . Zircons were then loaded back into their pre-cleaned micro-capsules with a microdrop of 7.5N HNO_3 and 70 μl concentrated HF. Samples were spiked with 6 – 8 mg of the EARTHTIME ^{202}Pb - ^{205}Pb - ^{233}U - ^{235}U tracer solution (ET2535; Condon et al., 2015; McLean et al., 2015) and dissolved in high-pressure Parr bombs at 210°C for >60 hours. Dissolved samples were dried down and redissolved in 6N HCl at 180°C for 12 hours to convert the samples to chlorides. The solutions were dried again and redissolved in 3N HCl in preparation of ion exchange chromatography. U and Pb were separated using an HCl-based ion exchange chemistry following procedures modified from Krogh (1973). The U-Pb fractions were dried down with a microdrop of 0.02 M H_3PO_4 and loaded onto zone-refined single Re filaments with one microdrop of a silica gel emitter (Gerstenberger and Haase, 1997). All measurements were performed at the Institute of Petrology and Geochemistry at ETH Zurich employing a Thermo Scientific TRITON Plus thermal ionization mass spectrometer (TIMS). Pb was

measured sequentially on a dynamic MassCom secondary electron multiplier and U was measured in static mode as U-oxide using Faraday cups fitted with $10^{13} \Omega$ resistor amplifiers (von Quadt et al., 2016; Wotzlav et al., 2017). The linearity of the MasCom secondary electron multiplier was calibrated through repeated measurements of SRM982 over a range of intensities up to 1.4 Mcps. Instrumental mass fractionation was corrected by calculating the deviation of the measured $^{202}\text{Pb}/^{205}\text{Pb}$ and $^{233}\text{U}/^{235}\text{U}$, respectively, from the known tracer composition of the ET2535 tracer solution (ET2535 v 3.0; Condon et al., 2015; McLean et al., 2015), and assuming a sample and blank $^{238}\text{U}/^{235}\text{U}$ of 137.818 ± 0.045 (2σ ; Hiess et al., 2012). Comparison with total procedural blank measurements indicated that analyzed zircons did not contain common Pb and that all common Pb in the zircon analyses were derived from the laboratory blank. All common Pb in zircon analyses was therefore corrected using the long-term average laboratory blank composition of $^{206}\text{Pb}/^{204}\text{Pb} = 18.40 \pm 0.20$, $^{207}\text{Pb}/^{204}\text{Pb} = 15.19 \pm 0.19$ and $^{208}\text{Pb}/^{204}\text{Pb} = 36.93 \pm 0.45$ (1σ abs; $n=16$). Data reduction and error propagation of the U-Pb data was carried out using Tripoli and U-Pb Redux software (Bowring et al., 2011) applying the algorithms of McLean et al. (2011). U-Pb ages were calculated relative to the EARTHTIME tracer calibration v. 3 (Condon et al., 2015) and the U decay constants of Jaffey et al. (1971). All uncertainties of U-Pb ages are reported at the 95% confidence interval (2σ) and do not include decay constant uncertainties. Results of analyses of ET2535 spiked aliquots of the EARTHTIME 100 synthetic solution (Condon et al., 2015) as well as analyses of zircon reference materials performed over the course of this study are reported in von Quadt et al. (2016) and Wotzlav et al. (2017).

All $^{206}\text{Pb}/^{238}\text{U}$ dates were corrected for initial ^{230}Th - ^{238}U disequilibrium in the ^{238}U - ^{206}Pb decay chain (e.g., Schärer, 1984) using a constant Th/U partition coefficient ratio assuming that variations in Th/U of the zircons result from different Th/U of the melt in equilibrium during zircon crystallization and not from variations in relative zircon-melt partitioning of Th and U. Especially for young zircons the correction for initial ^{230}Th disequilibrium is crucial with the magnitude of the correction significantly exceeding analytical uncertainties (Crowley et al., 2007). Accurate correction requires knowledge of the Th/U ratio of the Zircon ($\text{Th}/\text{U}_{\text{zircon}}$) and the Th/U ratio of the crystallizing melt ($\text{Th}/\text{U}_{\text{melt}}$). For this study, a constant $D_{\text{Th}/\text{U}}$ of 0.25 ± 0.10 (e.g., Rubatto and Hermann, 2007) is used for all zircons, which is in agreement with the approach used in a number of recent high precision geochronological studies on Neogene zircons (e.g., Barboni and Schoene, 2014; Wotzlav et al., 2014; Buret et al., 2016).

Solution Hf isotope analysis

Analyses of Hf-isotopes were conducted on selected zircon fragments that were dated by CA-ID-TIMS employing solution nebulization MC-ICP-MS. The Zr-Hf and trace element fraction (“wash”) was collected during U-Pb column chemistry and Hf was separated from the other elements by ion-exchange column chromatography to eliminate isobaric interferences from Yb and Lu. Isotopic Hf-analysis was conducted using a Nu Plasma II MC-ICP-MS at the Institute of Geochemistry and Petrology, ETH Zürich (Buret et al., 2016). Liquids were aspirated into the plasma through a DSN-100 desolvation nebulizer with an uptake rate of $50 \mu\text{l}/\text{min}$. Data collection was by Faraday detectors in a static mode

with 50 integration cycles over seven minutes followed by a washout with HNO₃ and trace Hf mixture. Measured ¹⁷⁶Hf/¹⁷⁷Hf values were normalized to a 15 ppb JMC 475 standard solution (¹⁷⁶Hf/¹⁷⁷Hf = 0.282160; Vervoort and Blichert-Toft, 1999) that was measured after every six zircon measurements. Repeat analyses of the standard solution over three analytical session yielded values of 0.282153 ± 12 (*n* = 11) 0.282187 ± 14 (*n* = 36) 0.282168 ± 14 (*n* = 25; uncertainties are given as 2SD). The ¹⁷⁶Lu decay constant of Scherer et al. (2001) and the ¹⁷⁶Lu/¹⁷⁷Hf derived from Lu/Hf measured by LA-ICP-MS were used to correct for minor ingrowth of ¹⁷⁶Hf by the decay of ¹⁷⁶Lu. Initial ¹⁷⁶Hf/¹⁷⁷Hf ratios and ε_{Hf} were calculated using an age of 1.2 Ma and the CHUR parameters of Bouvier et al. (2008). All uncertainties are reported at the 2 sigma level and include within-run precision of each measurement and the reproducibility of the JMC 475 standard.

Results

Optical appearance and internal textures of zircons from SEM-CL

All zircons in the heavy mineral fraction were euhedral to subhedral with aspect ratios between 1:1 and 1:4 and lengths between 100 and 500 μm (Fig. 11). Most grains were pinkish but lost their color during annealing. Inherited cores, and mineral and melt inclusions could be identified in transmitted light. For zircon mounts no special selection was made based on appearance or inclusions to avoid any initial bias. Cathodoluminescence images can reveal inherited cores showing resorption features or detrital rounding surfaces (e.g. Fig. 11A, 11D, 11F). Zircons from Ok Tedi are typically oscillatory zoned or unzoned (Fig. 11A, 11D, 11E). Some zircons from the Fubilan porphyry and the intrusive breccias as well as all Pleistocene zircons from Anju, exhibit irregular planar zoning similar to sector zoning (Fig. 11A, 11B, 11C, 11F). Locally, these zones are overgrown by zircon with oscillatory zoning or no zoning (Fig. 11A, 11B).

Trace element distribution in zircons

Results of *in situ* trace element analysis by LA-ICP-MS are illustrated in Figure 12. Analysis of zircon cores and rims (based on CL images) allows us to track relative changes in trace element composition of the host melt during zircon crystallization. Zircon trace element compositions distinguish two significantly different zircon populations (Fig. 12A, 12B): One population, accounting for the majority of zircons, shows systematic core-rim variations consistent with changing melt composition induced by fractional crystallization of a titanite-bearing mineral assemblage (cf. Wotzlaw et al., 2013; Buret et al., 2016; Loader et al., 2017) and a smaller population with very low Th/U and Hf/Y showing no pronounced core-rim variations. These two populations are particularly well discriminated by their significantly different Th/U ratios and are therefore referred to as high-Th/U zircons (the majority of the zircons) and low Th/U zircons (the smaller sub-population).

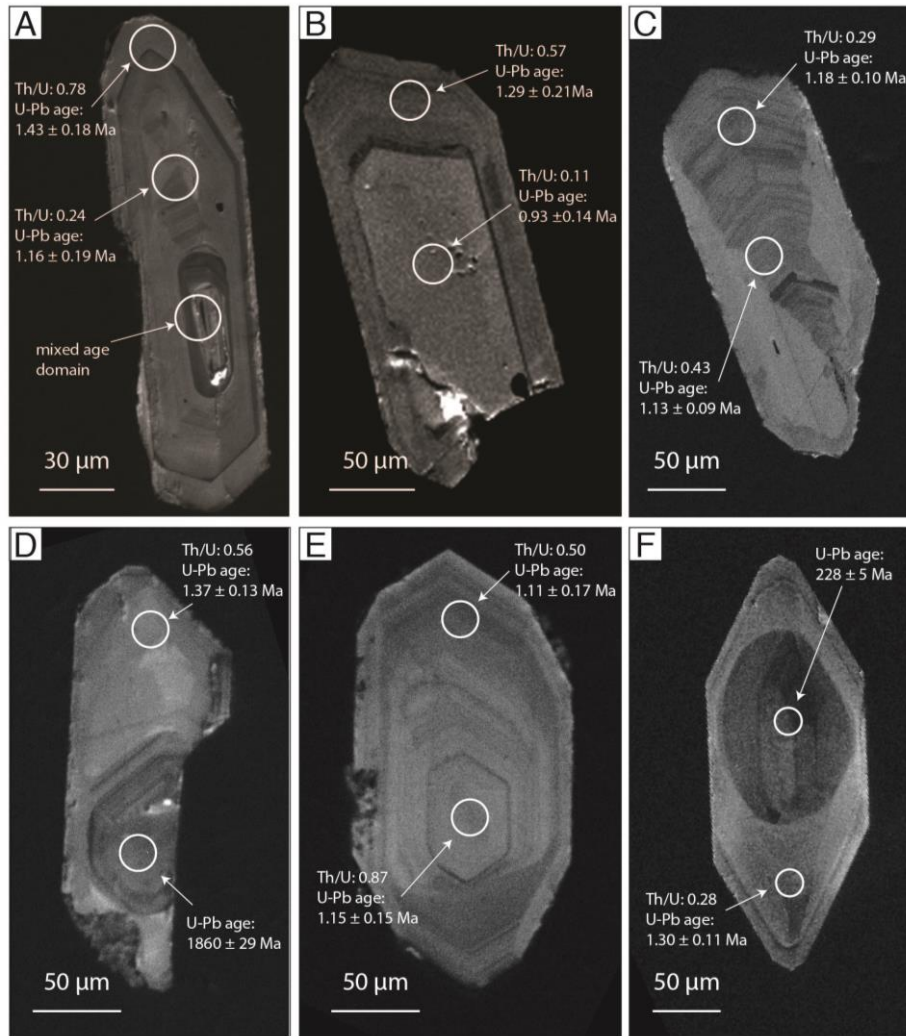


Figure 11. Cathodoluminescence images of selected zircons. **A, B:** Zircons showing high Th/U rims over low Th/U interior domains. Zircon in (A) contains a Proterozoic inherited core overgrown by the two chemically distinct Pleistocene zircon domains. **C:** Zircon displaying irregular sector zoning observed in some low Th/U zircons. **D:** Zircon with inherited core and Pleistocene overgrowth. **E:** Oscillatory zoning in zircons of the high Th/U population. **F:** Zircon from the Anju andesite with resorbed Mesozoic core overgrown by Pleistocene zircon without clear zoning. Circles indicate spots selected for LA-ICP-MS analyses. Crystallization ages for Pleistocene and Mesozoic domains are $^{206}\text{Pb}/^{238}\text{U}$ dates. Proterozoic ages are $^{207}\text{Pb}/^{206}\text{Pb}$ dates. Analysis of the inherited core in (A) resulted in a mixed and discordant age with an upper intercept pointing to a Proterozoic age of the core.

Zircons of the high-Th/U population (circles in all co-variation diagrams) occur in all samples from the Ok Tedi intrusive complex, except the Anju andesite. This population shows a steady decrease in Th/U and increase in Yb/Nd, Yb/Dy and Ce/Dy from cores to rims (Fig. 12) and systematic variations between the different samples. The equigranular diorite and biotite diorite show the least differentiated compositions (e.g., highest Th/U, lowest Hf/Y) whereas the trace element signatures of zircons from the monzodiorites, the Fubilan porphyry and the intrusive breccia suggest progressively later crystallization from an evolving magma reservoir (e.g., progressively lower Th/U, higher Hf/Y). These geochemical trends are consistent with closed-system fractionation of a titanite±hornblende±apatite-bearing mineral assemblage (Reid et al., 2011; Wotzlaw et al., 2013; Buret et al., 2016; Loader et al., 2017).

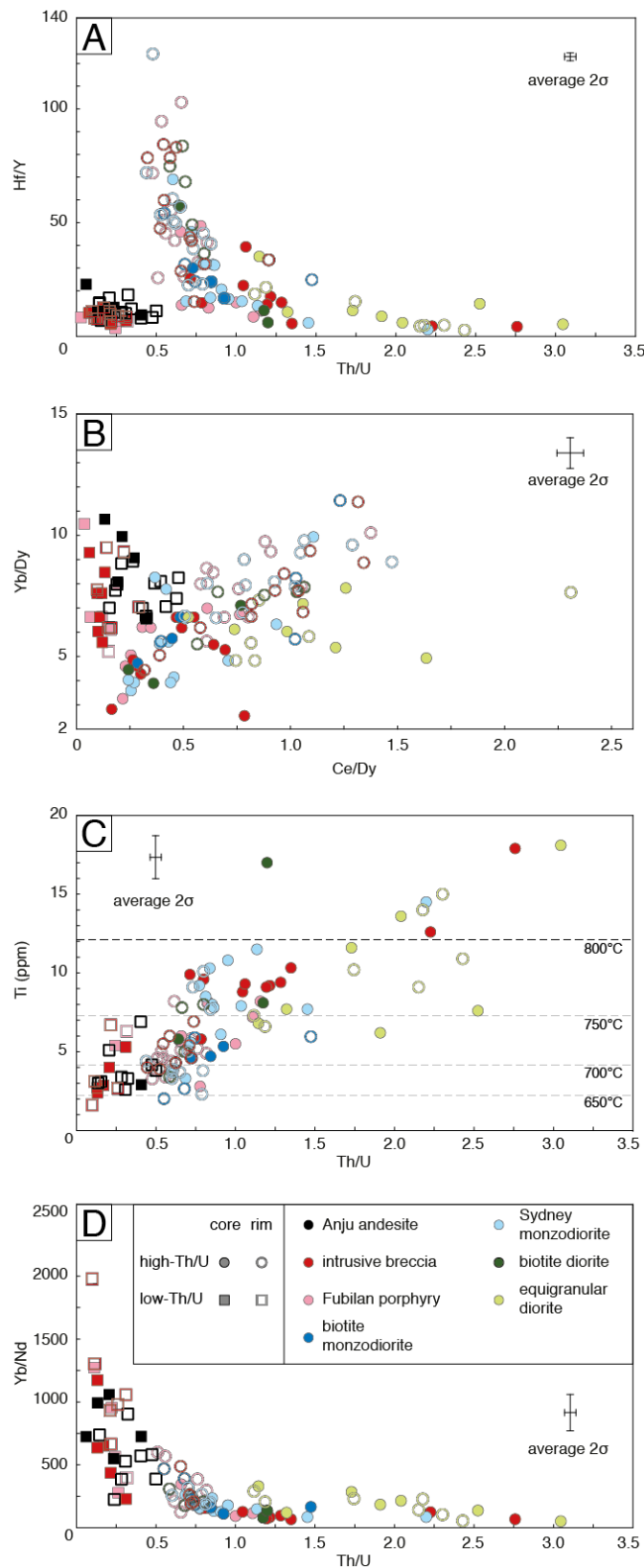


Figure 12. LA-ICP-MS trace element data for cores and rims of zircon grains from Ok Tedi. For clarity, only LA-ICP-MS analyses of zircons that were subsequently dated by ID-TIMS are plotted. The high Th/U domains show the same core-rim relationships for all samples (A-D). The low Th/U domains, only identified in zircons from the Fubilan porphyry and the intrusive breccia, plot as a distinct population without clear core-rim zonation (A, B). Average 2 sigma uncertainties are given. Temperature lines in (C) correspond to model zircon crystallization temperatures calculated from Ferry and Watson (2007) with $a\text{SiO}_2 = 1$ and $a\text{TiO}_2 = 0.7$.

Titanium-in-zircon thermometry (Watson and Harrison, 2005; Watson et al., 2006; Ferry and Watson, 2007) permits the estimation of model zircon crystallization temperatures in evolving magmas (Claiborne et al., 2010; Reid et al., 2011; Chelle-Michou et al., 2014; Dilles et al., 2015; Buret et al., 2016; Lee et al., 2017). Crucial for the accuracy of these temperatures is knowledge of the activities of SiO_2 (a_{SiO_2}) and TiO_2 (a_{TiO_2}) in the magma. We here apply an a_{SiO_2} of 1 based on the presence of quartz in all analyzed samples and estimate a_{TiO_2} to be 0.7 based on the occurrence of titanite (e.g., Chelle-Michou et al., 2014) in all Ok Tedi samples. The TiO_2 activity is the least constrained variable in granitoids (cf. Chelle-Michou et al., 2014; Lee et al., 2017). Changing a_{TiO_2} by 0.2 results in a change in the model zircon crystallization temperature by $\pm 30^\circ\text{C}$ while relative changes between zircons remain rather constant. Zircons that record high crystallization temperatures (i.e. $>800^\circ\text{C}$) most likely crystallized from a magma that was not saturated in SiO_2 . Undersaturation of the melt with respect to SiO_2 results in a slight overestimation of the zircon crystallization temperatures ($\sim 25^\circ\text{C}$ for a $a_{\text{SiO}_2} = 0.8$ and Ti-concentrations >10 ppm). Even when accounting for these systematic uncertainties associated with the Titanium-in zircon thermometer in obtaining absolute crystallization temperatures, it is a valuable tool to compare relative crystallization temperature changes in zircon datasets.

All high-Th/U zircons show a general down-temperature evolution from cores to rims from maximum temperatures of $>800^\circ\text{C}$ in zircons from the equigranular diorite and biotite diorite to minimum temperatures of 640°C in the four main intrusions at Ok Tedi (Fig. 12C). This down temperature trend is in accordance with a gradually cooling magmatic system over time. The low-Th/U zircons occur as a minor population within the youngest samples of the Ok Tedi complex, i.e. the Fubilan porphyry and the intrusive breccia. Pleistocene zircons of equivalent composition also occur in the Anju andesite that was sampled ~ 10 km south west of the Ok Tedi complex (see Fig. 2 for location). Planar and sector zoning (Fig. 11B, 11C, 11F) in this zircon population is revealed by CL images in contrast to the predominantly oscillatory zoned or unzoned high-Th/U zircons (Fig. 11E). Some low-Th/U cores are overgrown by high-Th/U rims but the opposite is not observed (see Fig. 11A, 11B). In addition to the characteristically low Th/U ratios (<0.5), these zircons also display systematically lower Hf/Y ratios (<25), are enriched in U ($>1,000$ ppm), depleted in Hf ($<9,000$ ppm), depleted in LREE and have higher Yb/Nd ratios. Core-rim variations are less pronounced compared to the high-Th/U zircons but a progressive increase in Ce towards the rims is observed in most of these zircons.

Ti-concentrations in these zircons are mostly below 7 ppm indicating crystallization temperatures $<750^\circ\text{C}$ of this zircon population.

Europium anomalies ($\text{Eu}/\text{Eu}^* = \text{Eu}_N/(\text{Sm}_N \times \text{Gd}_N)^{1/2}$) in zircons have been used as a redox indicator of the crystallizing magma and were inferred to be related to fertility regarding hydrothermal ore formation (e.g. Chelle-Michou et al., 2014; Dilles et al., 2015; Lee et al., 2017). Recently, it was suggested that these anomalies might not solely reflect redox conditions but can be largely influenced by co-crystallizing REE-bearing mineral phases, especially titanite (Loader et al., 2017). Titanite is common in magmatic rocks associated with porphyry deposits (e.g. Chelle-Michou et al., 2014; Buret et al., 2016; Loader et al., 2017) and therefore might convolute the seemingly characteristic low europium anomalies that were

attributed to highly oxidizing conditions. We refrain from discussing the relevance of europium anomalies for the redox conditions and ore fertility and simply note that values vary rather unsystematically between 0.5 and 1.0 (Digital Appendix).

Spatially resolved low precision U-Pb dates

In situ geochronology by LA-ICP-MS on Pleistocene zircons with average to low U-contents results in uncertainties of up to 30% in $^{206}\text{Pb}/^{238}\text{U}$ dates. Nevertheless, *in situ* dates are important to select zircons without inherited cores for ID-TIMS analysis. Pleistocene zircons from the Anju andesite were not dated by CA-ID-TIMS; however, LA-ICP-MS dating yielded a weighted mean $^{206}\text{Pb}/^{238}\text{U}$ date of 1.107 ± 0.047 Ma ($n = 18$; MSWD = 2.9; see Digital Appendix).

The age distribution of the inherited component fingerprints the crustal component that was assimilated by the underlying magma reservoir, possibly already in the lower crust (e.g., Chelle-Michou et al., 2014). Age determinations by LA-ICP-MS show that approximately 30% of the zircons are inherited or contain inherited cores. In many cases, these inherited cores are overgrown by zircon rims of Pleistocene age. The age distributions of the inherited zircons and zircon cores are very similar for all investigated intrusive rocks, always showing two main age populations; a smaller Mesozoic component (320 – 180 Ma) and a predominant component of Proterozoic age (2.2 – 1.6 Ga; see Fig. 13).

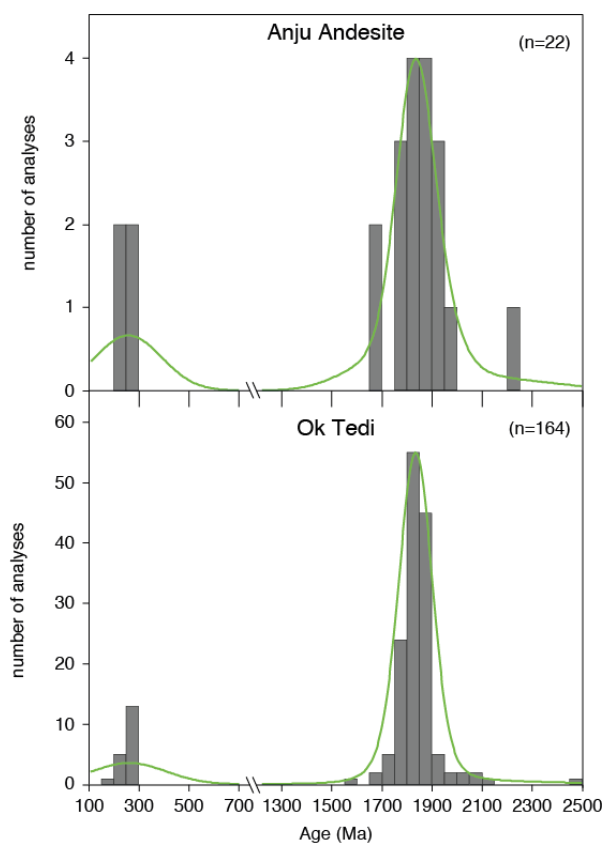


Figure 13. Histograms and kernel density estimates illustrating the age distribution of inherited zircon domains from LA-ICP-MS analyses. Concordant $^{206}\text{Pb}/^{238}\text{U}$ dates are given for Mesozoic zircons. $^{207}/^{206}\text{Pb}$ dates are used for Proterozoic zircon domains. Note the similarity of the age distributions of inherited zircons for the Ok Tedi intrusions and the Anju andesite.

High-precision CA-ID-TIMS U-Pb ages

We dated between 12 and 19 zircons from each of the four main intrusions, seven from the equigranular diorite, and four zircons from the biotite diorite (Fig. 14). All eleven zircons from the diorite samples crystallized within the same maximum period of 52 ± 25 kyr. The youngest zircon of the equigranular diorite yielded a $^{206}\text{Pb}/^{238}\text{U}$ age of 1.349 ± 0.011 Ma, whereas the youngest dated zircon of the biotite diorite yielded a statistically equivalent $^{206}\text{Pb}/^{238}\text{U}$ age of 1.330 ± 0.023 Ma, which we interpret to define the time of emplacement of these diorite intrusions. Zircons of the Sydney and biotite monzodiorite display a mutually similar but more extended age distributions recording 137 ± 42 kyr of zircon crystallization, with the oldest zircons yielding crystallization ages equivalent to the diorites. We take the youngest zircon crystallization ages of 1.269 ± 0.030 Ma and 1.262 ± 0.020 Ma, respectively, as an estimate for the age of emplacement. This suggests that these two monzodiorite intrusions were emplaced, some 60 ± 38 kyr after the diorites, within a very short time interval that is unresolvable even by ID-TIMS techniques.

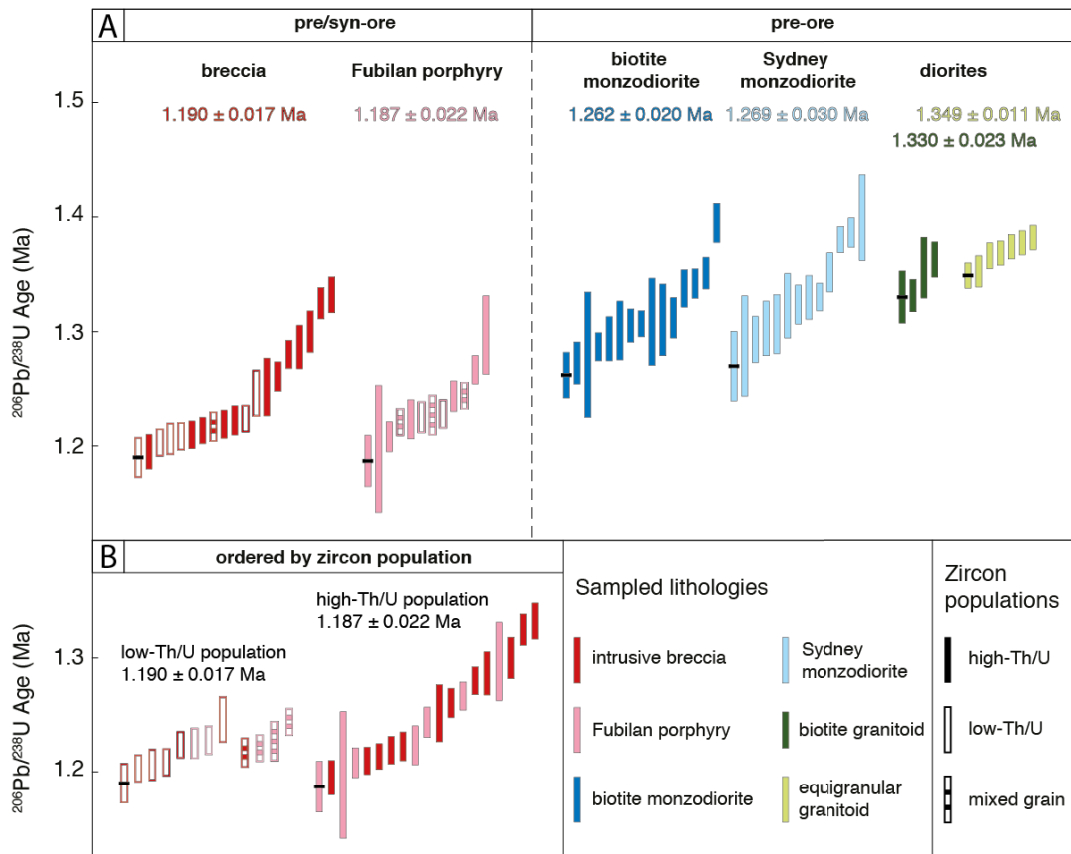


Figure 14. Age ranked plot showing $^{206}\text{Pb}/^{238}\text{U}$ dates of individual zircons from all rocks analyzed by ID-TIMS. Zircons are ordered by sample in (A) and re-ordered by chemical population (B; see text for details). The youngest dated zircon of each sample is considered as the best estimate of the emplacement age of the respective magmatic rock and is shown numerically in (A). The diorites are the oldest intrusions followed by the emplacement of the monzodiorites ~ 80 kyr later. The Fubilan porphyry and the intrusive breccia were emplaced ~ 70 kyr after the monzodiorites. The emplacement ages of the latter are overlapping within analytical uncertainty indicating rapid emplacement of these two units. Zircons from the Fubilan porphyry and the intrusive breccia are grouped by chemical population in (B). The youngest crystallization ages of the low Th/U zircons and the high Th/U zircons overlap within uncertainty (see text for discussion).

$^{206}\text{Pb}/^{238}\text{U}$ dates of analyzed zircons from the Fubilan porphyry ($n=12$) and the intrusive breccia ($n=19$) display similar age distributions recording 110 ± 41 kyr and 142 ± 23 kyr of zircon crystallization, respectively. The youngest dated zircons of the Fubilan porphyry and of the intrusive breccia yielded statistically equivalent $^{206}\text{Pb}/^{238}\text{U}$ dates of 1.187 ± 0.022 Ma and 1.190 ± 0.017 Ma. Dates from the Fubilan porphyry and the intrusive breccia suggest that their emplacement occurred 70 ± 30 kyr after the emplacement of the monzodiorites.

The two chemically distinct zircon populations occur in both the Fubilan porphyry and in the intrusive breccia. The age spectrum of the normal high-Th/U zircon population reaches back to the earliest ages ($\sim 110 - 140$ kyr before emplacement) suggesting an antecrystic component in these zircons (Miller et al., 2007). The anomalous low-Th/U zircons grew exclusively in a later part of the age range, within the last 56 ± 26 kyr before emplacement of both rock types. As discussed later, the temporal overlap of the high- and anomalous low-Th/U zircon populations indicates concurrent zircon crystallization from two geochemically substantially contrasting magma reservoirs.

These CA-ID-TIMS U-Pb dates establish a precise temporal sequence for the emplacement of the Ok-Tedi intrusive complex, by clearly resolving successive emplacement ages based on the youngest zircons in each lithology. On the other hand the zircon crystallization ages span a continuum, in which overlapping age distributions correlate with a continuous trends in zircon trace element compositions. This is best illustrated by the systematic decrease in Th/U (from TIMS analyses) with time (Fig. 15A). This trend can be subdivided into two intervals with different slopes in age vs. Th/U space (Fig. 15A). Zircons from the equigranular diorite and biotite diorite reveal a decrease in Th/U from 2.3 to 1.2 over a short time interval of 62 ± 25 kyr. High-Th/U zircons from the monzodiorites, Fubilan porphyry and intrusive breccia display a decrease in Th/U from 1.3 to 0.5 within a time interval of 212 ± 43 kyr. The anomalous low-Th/U zircons appear to represent the continuation of this trend based on this element ratio alone, but other trace elements reveal that this population is not derived from the high-Th/U population (see above and Fig. 12).

Hf isotope data from zircon

All Hf isotope analyses cluster between ϵHf values of -5 and -11, without clear correlations with age or other chemical parameters, reflecting a similar degree of assimilation of crustal rocks by mantle-derived magmas (Fig. 15B).

Discussion

Origin and tectonic setting of the Ok Tedi igneous complex

The Hf isotope ratios of autocrystic zircons and the age and geochemistry of inherited zircons characterize the degree of assimilation and the type of assimilant contributing to a common parental magma sourcing the porphyritic stocks in the Ok Tedi complex and the magma reservoir from which the low Th/U zircons crystallized. The ϵHf isotopic values in all Pleistocene zircons scatter non-systematically from -11 to -5 with most of the data overlapping within error. This

indicates locally slightly different but generally similar degrees of assimilation of the magma chamber with the wall-rock (Fig. 15B). A previous study by van Dongen et al. (2010a) characterized the inherited Proterozoic zircons by endmember ϵ_{Hf} values of ~ -43 and obtained a similar range to our results for the Pleistocene zircons.

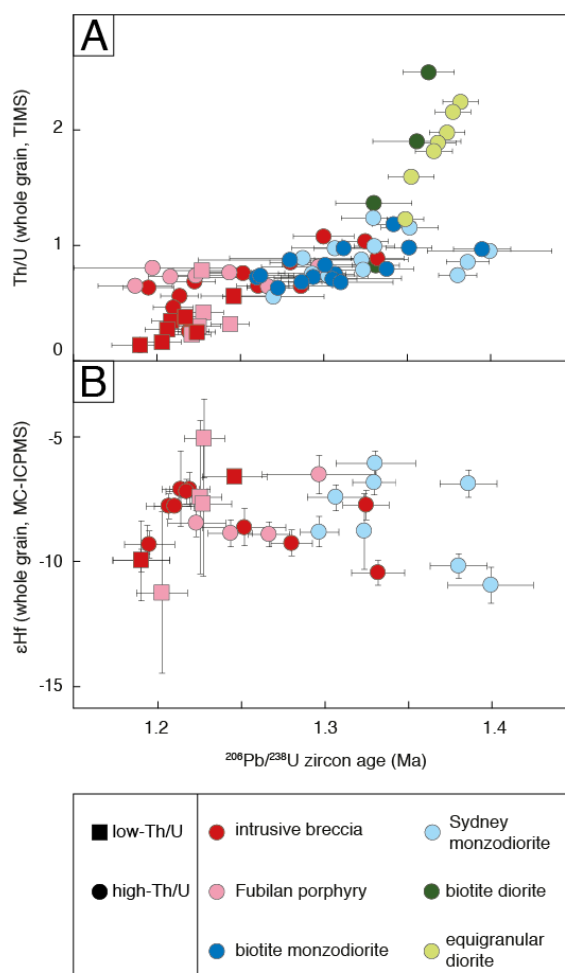


Figure 15. Th/U and ϵ_{Hf} -values plotted as a function of time. High Th/U zircons are plotted as circles and low Th/U zircons or mixed grains are plotted as squares. Th/U of high Th/U zircons systematically decreases with time while ϵ_{Hf} -values do not show any systematic correlation. The low Th/U population does not show clear relationships between trace element chemistry or Hf isotopic composition with time.

The majority of inherited zircons from Ok Tedi intrusions are Proterozoic with the population mode between 1.9 – 1.8 Ga (Fig. 13). This is in accordance with the inherited population described by van Dongen et al. (2010a), who described these zircons as being directly or erosinally derived from basement rocks similar to the Mount Isa Inlier. Another possibility is that they crystallized during the Halls Creek orogeny (Kueter et al., 2016). In this study, we additionally identified a significant number of Mesozoic (i.e. 300 – 200 Ma) zircons that are concordant in age (Fig. 13 and supplementary material), suggesting that the large underlying magma reservoir is hosted by sedimentary rocks containing both Mesozoic and Proterozoic inherited zircon populations.

The Tasman line, a suture dividing Proterozoic basement in the west from Mesozoic basement in the east throughout Australia, is suggested to run approximately north-south through Papua New Guinea (Fig. 1). The exact location

of the Tasman line through Papua New Guinea is debated (e.g., Davies, 2012) but our data suggest that zircons were derived from both sides of the Tasman line. The fact that the majority of inherited zircons are Proterozoic suggests that Ok Tedi is still underlain by Proterozoic basement and that the Tasman line runs east of the deposit.

The Ok Tedi intrusions as well as the Anju andesite show the same distribution of inherited zircon ages pointing to a similar assimilated in both intrusions (Fig. 13). Previous geochronological investigations of the Ok Tedi intrusive complex using different techniques resulted in similar ages: however, with lower resolution compared to this study. Van Dongen et al. (2010a) obtained U-Pb zircon ages using SHRIMP that range from 1.4 – 1.1 Ma. Their ages for individual samples are systematically younger by approximately 70 kyr compared to ages obtained in this study. We suggest that this discrepancy may be due to an inadequate correction for initial Th-U disequilibrium, as also addressed by Holm (2013). Page (1975) obtained K-Ar ages on biotite from intrusive rocks at Ok Tedi, and interpreted mineralization to have occurred at 1.2 – 1.1 Ma. The Anju andesite was dated at 0.97 ± 0.06 Ma by K-Ar dating on hornblende close to our age of 1.107 ± 0.047 obtained by U-Pb dating by LA-ICP-MS. These ages indicate magmatic activity at the Anju intrusive center roughly contemporaneously with the Ok Tedi complex, but were not precise enough to resolve age differences and assess the duration of magmatic-hydrothermal activity

Evolution of the Ok Tedi magma reservoir recorded by zircon

Major mineral phases such as plagioclase and amphibole are important carriers of specific trace elements (e.g., Sr in plagioclase). However, the budget of many other trace elements in silicic magmas is controlled by crystallization of accessory minerals such as apatite, zircon and titanite due to their high and distinct partition coefficients (e.g. Bachmann et al., 2005; Rubatto and Hermann, 2007). Progressive crystallization of such mineral phases results in characteristic trace element signatures in the residual magma. In particular, trace element ratios such as Th/U, Hf/Y or Yb/Dy have been used as a tracer for the degree of magma differentiation (e.g. Wotzlaw et al., 2013; Samperton et al., 2015; Buret et al., 2016). These signatures are recorded by the concurrently crystallizing zircon crystals, which thereby track the chemical evolution of the magma on a precisely dated timeline (e.g., Reid et al., 2011; Schoene et al., 2012; Wotzlaw et al., 2013; Samperton et al., 2015; Buret et al., 2016).

Pleistocene zircons of the high-Th/U population occur in all investigated samples from Ok Tedi, with the notable exception of the Anju andesite, and are interpreted to record the chemical evolution of the main magma reservoir underlying and driving Ok Tedi. These zircons display systematic variations in trace element geochemistry between the different units and consistent core-to-rim trends characterized by a decreasing Th/U ratio and increasing Hf/Y, Yb/Nd, Yb/Dy, Ce/Dy ratios (Fig. 12). These variation trends can be readily explained by changes in melt composition induced by closed system fractional crystallization of a phenocryst assemblage including titanite and apatite (Fig. 7A). This interpretation is also consistent with decreasing Ti-in-zircon temperatures from the diorites to the Fubilan porphyry and intrusive breccia (Fig. 12C) indicating progressive cooling and crystallization of an upper-crustal reservoir that remained largely

unaffected by any chemical or thermal rejuvenation. A progressively evolving magma is also consistent with observations of decreasing anorthite contents from more basic plagioclase in the monzodiorites towards more albitic plagioclase in the Fubilan porphyry (Bamford, 1972). Our interpretation of the zircon trace element variations seen in our *in situ* LA-ICP-MS data is further reinforced by the continuous decrease of whole grain Th/U with time (Fig. 15A).

Zircon U-Pb dates record a total duration of crystallization of 212 ± 44 kyr within the upper crustal magma reservoir. The first magmas that were extracted from the magma reservoir and emplaced at shallow crustal levels are represented by the two diorites. Zircons from the diorites record 52 ± 25 kyr of magma evolution after zircon saturation. Extraction of the diorites was followed by 60 ± 38 kyr of closed-system fractional crystallization until extraction and shallow emplacement of the monzodiorites that record an intermediate stage in the evolution of the underlying reservoir. Emplacement of the intrusive breccia and the Fubilan porphyry occurred 75 ± 30 kyr after emplacement of the monzodiorites, that in turn postdated diorite intrusion by 60 ± 38 kyr. It is possible that additional intrusions at depth or unrecognised subdivisions may have intruded between these recognised and time-resolved events. However, if these events occurred they did not disturb the geochemical fractional crystallization trend in the magma reservoir, as they did not leave any record in the zircon trace element geochemistry. A further 75 ± 30 kyr of continued closed-system fractional crystallization is recorded in the high-Th/U zircons of the Fubilan porphyry and the intrusive breccia. The Fubilan porphyry and the intrusive breccia were then emplaced, nearly contemporaneously and concurrently with Au-Cu mineralization within dating uncertainties of ~ 20 kyr, terminating the record of magmatic activity at Ok Tedi.

The origin of the anomalous low Th/U zircon population

Four different scenarios can be envisaged to result in the homogenous but very distinct low Th/U zircon compositions: (1) crystallization in separate magma batches within the same reservoir, (2) contamination of melt pockets by wall-rock, (3) hydrothermal zircon growth, (4) or zircon growth in a different magma reservoir than the high Th/U population and later mixing.

Zircon crystallization in physically separated magma batches within the same reservoir would not result in two chemically different zircon populations. In this scenario, zircon geochemistry could vary measurably with time but would still show systematic trends (e.g., Bajo de la Alumbrera: Buret et al., 2016).

Contamination of melt pockets by melting of lower-crustal wall-rock should result in a systematic digression in the Hf-isotope composition of the melt and therefore, the zircons. However, ϵ_{Hf} of the low-Th/U zircon population shows the same scatter as the high-Th/U zircon population and actually includes the highest and lowest individual values (Fig. 15B).

The zircon record at Ok Tedi gives no evidence for zircon growth from an aqueous fluid. Hydrothermal zircon is expected to form distinct overgrowth over magmatic zircon (Schaltegger, 2007) and is unlikely to be overgrown by magmatic zircon, as observed in some of our low-Th/U zircons. Furthermore, reported Th/U ratios (>0.5 and often $\gg 1$) and Ti-contents ($\gg 50$ ppm) in hydrothermal zircons are

typically much higher than observed here (McNaughton et al., 2005; Hoskin, 2005).

The fourth scenario of crystallization in a different magma reservoir and a late-stage mixing event appears to be the most plausible. It readily explains why the two distinct zircon populations only recorded the end of the magmatic history and why low-Th/U zircons are sometimes overgrown by high-Th/U zircon (Fig. 11). Furthermore, the magmatic zircon population identified from the Anju andesite is strikingly similar to the low-Th/U zircon population, demonstrating the presence of a suitable, somewhat more mafic magma only a few kilometers away from the Ok Tedi magmatic complex.

Late-stage magma mixing triggering porphyry emplacement, brecciation and Au-Cu mineralization

If we accept magma mixing as the most likely explanation for the distinct zircon populations in the two most intimately ore related lithologies, we conclude that extraction and emplacement of the Fubilan porphyry and the intrusive breccia was preceded by a late-stage magma-mixing event, which brought together two magmas containing distinct zircon populations. Crystallization ages of the low-Th/U zircons span a narrow age range of 56 ± 26 kyr temporally overlapping with the younger of the normal high-Th/U zircons within the same samples. This suggests that the two zircon populations crystallized simultaneously from separate magma batches before these were mixed; otherwise the two chemical signatures would become blurred. The $^{206}\text{Pb}/^{238}\text{U}$ dates of the youngest dated zircons of both chemical populations in both rock samples overlap within uncertainty, suggesting that the two magma batches co-existed until shortly (<30 kyr) before extraction of the Fubilan porphyry and the intrusive breccia. After injection of the inferred andesitic magma with anomalous low-Th/U zircons into the main dacitic magma reservoir, some low-Th/U zircons resided long enough in this main magma reservoir to be overgrown by high-Th/U rims before the Fubilan porphyry was extracted from this reservoir, but not long enough for the chemical signatures of the two magmas to become mixed and crystallize a zircon population of intermediate chemical signature. The fact that the consistent fractional crystallization trend of the high Th/U zircons continues undisrupted indicates that the injected magma containing the low Th/U zircons was volumetrically minor. Fractional crystallization of large magma chambers has commonly been considered essential for massive fluid generation and ore formation (Cline and Bodnar 1991; Chambefort et al., 2013; Lee et al., 2017). Our data provide a direct, time-resolved record of a long-lived evolution via fractional crystallization of a single large magma volume. Other studies suggested late-stage interaction of different magmas (i.e., mafic underplating, magma recharge, mixing with crustal melts etc.) in porphyry copper systems (Tapster et al., 2016; Buret et al., 2016; Buret et al., 2017; Lee et al., 2017). These studies together with previous evidence from silicate and sulfide melt inclusions (Halter et al., 2005) and magma mingling textures (Hattori and Keith, 2001) indicate that such recharge events are an essential prerequisite for porphyry formation and mineralization. Our data tightly constrain the timing of final injection of a distinct magma batch, possibly similar in composition to the Anju andesite host magma, into a large and highly

fractionated and evolved magma reservoir underlying the Ok Tedi deposit. The close temporal association between magma injection and porphyry-ore formation strongly suggests that the injection is the trigger for the late stage evolution of the magmatic-hydrothermal system including porphyry intrusion, breccia emplacement and Au-Cu mineralization as the last short-lived event in the considerably longer lifetime of an upper-crustal magma chamber.

Conclusion

Our zircon trace element data and U-Pb geochronology of the intrusive suite associated with the Ok Tedi Au-Cu deposit reveal a high-precision record of the pre-mineralization evolution of a fertile magma reservoir. The reservoir from which the porphyry intrusions at Ok Tedi were extracted evolved by closed system fractional crystallization over 212 ± 44 kyr. Within this magma chamber life, all of the intrusions in the Ok Tedi intrusive complex were extracted and emplaced at the present mine level in three main pulses, separated by two clearly resolvable age gaps of 60 ± 38 kyr and 75 ± 30 kyr. The first pulse was essentially barren and occurred prior to major fluid saturation in the magma chamber. The second pulse emplaced monzodiorites cut by largely barren stockwork veins, but probably formed much of the skarn and possibly some of the skarn-hosted Au-Cu mineralization. Porphyry Au-Cu mineralization as well as ore formation associated with intrusive breccias occurred during the last of these three porphyry emplacement events. A chemically distinct zircon population, occurring exclusively in the youngest igneous rocks, is attributed to a late stage event of magma recharge and mixing, just prior (<30 kyr) to the emplacement of the strongly mineralized porphyry and intrusive breccia. This precisely dated geochemical event indicates that mafic magma injection into a large and slowly crystallizing magma reservoir was the immediate trigger for most or all economic Au-Cu mineralization at Ok Tedi.

Our study confirms and sharpens the conclusion from other recent high-precision geochronology studies regarding distinct lifetimes of porphyry ore systems at different spatial scales. The thermal lifetime of large upper-crustal magma reservoirs as the source of ore fluids and all ore forming components typically lasts a few hundred thousand years, determined by the rate of cooling of the magma chamber. The duration of one or several events of porphyry emplacement and hydrothermal Au-Cu mineralization is much shorter, spanning a range of tens of thousands of years in total, with even shorter durations of individual magma and fluid pulses determined by the rate of fluid extraction from the magma chamber.

Acknowledgements

This work has been supported by Swiss National Science Foundation Grant 200026-166151. J.-F. Wotzlaw acknowledges funding through the ETH Zürich Postdoctoral Fellowship program. Remy Lüchinger and Peter Nievergelt are thanked for thin section preparation and imaging. The authors are grateful for help by Y. Buret with Hf isotopic analyses. Access to the SEM at the Department of Materials, ETH Zurich by André Röthlisberger and Karsten Kunze is kindly

acknowledged. Extensive logistical and field support by the Ok Tedi Mining Limited, especially by Daniel Hastings, Robert Smillie, Oscar Rarua, Isaka Bisanbasa and Richard Addo is greatly appreciated. Peter Pollard contributed valuable discussions and input to an earlier version of this manuscript. We appreciate constructive reviews by John Dilles, Sebastien Meffre and Evan Orovan and editorial handling by Pete Hollings and Evan Orovan.

References

Arnold, G., and Fitzgerald, F., 1977, Igneous rock types and their alteration, Mt Fubilan porphyry copper deposit: Geological Survey of Papua New Guinea, Report 77/5, 10 p.

Arnold, G., and Griffin, T. J., 1978, Intrusions and porphyry copper prospects of the Star Mountains, Papua New Guinea: *Economic Geology*, v. 73, p. 785–795.

Audétat, A., Pettke, T., Heinrich, C. A., and Bodnar, R. J., 2008, Special paper: the composition of magmatic-hydrothermal fluids in barren and mineralized intrusions: *Economic Geology*, v. 103, p. 877–908.

Bachmann, O., Dungan, M., and Bussy, F., 2005, Insights into shallow magmatic processes in large silicic magma bodies: the trace element record in the Fish Canyon magma body, Colorado: *Contributions to Mineralogy and Petrology*, v. 149, p. 338–349.

Baldwin, S. L., Fitzgerald, P. G., and Webb, L. E., 2012, Tectonics of the New Guinea region: *Annual Review of Earth and Planetary Sciences*, v. 40, p. 495–520.

Bamford, R. W., 1972, The Mount Fubilan (Ok Tedi) porphyry copper deposit, Territory of Papua and New Guinea: *Economic Geology*, v. 67, p. 1019–1033.

Barboni, M., and Schoene, B., 2014, Short eruption window revealed by absolute crystal growth rates in a granitic magma: *Nature Geoscience*, v. 7, p. 524–528.

Black, L. P., Kamo, S. L., Allen, C. M., Aleinikoff, J. N., Davis, D. W., Korsch, R. J., and Foudoulis, C., 2003, TEMORA 1: a new zircon standard for Phanerozoic U–Pb geochronology: *Chemical Geology*, v. 200, p. 155–170.

Bouvier, A., Vervoort, J. D., and Patchett, P. J., 2008, The Lu–Hf and Sm–Nd isotopic composition of CHUR: constraints from unequilibrated chondrites and implications for the bulk composition of terrestrial planets: *Earth and Planetary Science Letters*, v. 273, p. 48–57.

Bowring, J., McLean, N. M., and Bowring, S., 2011, Engineering cyber infrastructure for U–Pb geochronology: Tripoli and U–Pb_Redux: *Geochemistry, Geophysics, Geosystems*, v. 12, p. 1–19

Buret, Y., von Quadt, A., Heinrich, C., Selby, D., Wälle, M., and Peytcheva, I., 2016, From a long-lived upper-crustal magma chamber to rapid porphyry copper emplacement: Reading the geochemistry of zircon crystals at Bajo de la Alumbrera (NW Argentina): *Earth and Planetary Science Letters*, v. 450, p. 120–131.

Buret, Y., Wotzlaw, J. F., Roozen, S., Guillong, M., von Quadt, A., and Heinrich, C. A., 2017, Zircon petrochronological evidence for a plutonic-volcanic connection in porphyry copper deposits: *Geology*, v. 45, p. 623–626.

Candela, P. A., 1989, Calculation of magmatic fluid contributions to porphyry-type ore systems: Predicting fluid inclusion chemistries: *Geochemical Journal*, v. 23, p. 295–305.

Cathles, L., 1977, An analysis of the cooling of intrusives by ground-water convection which includes boiling: *Economic Geology*, v. 72, p. 804–826.

Cathles, L., and Shannon, R., 2007, How potassium silicate alteration suggests the formation of porphyry ore deposits begins with the nearly explosive but barren expulsion of large volumes of magmatic water: *Earth and Planetary Science Letters*, v. 262, p. 92–108.

Chambefort, I., Dilles, J. H., and Longo, A. A., 2013, Amphibole geochemistry of the Yanacocha Volcanics, Peru: Evidence for diverse sources of magmatic volatiles related to gold ores: *Journal of Petrology*, v. 54, p. 1017–1046.

Chelle-Michou, C., Chiaradia, M., Ovtcharova, M., Ulianov, A., and Wotzlaw, J.-F., 2014, Zircon petrochronology reveals the temporal link between porphyry systems and the magmatic evolution of their hidden plutonic roots (the Eocene Corocchohuayco deposit, Peru): *Lithos*, v. 198, p. 129–140.

Cherniak, D. J., and Watson, E. B., 2003, Diffusion in zircon: *Reviews in Mineralogy and Geochemistry*, v. 53, p. 113–143.

Chiaradia, M., Schaltegger, U., Spikings, R., Wotzlaw, J. F., and Ovtcharova, M., 2013, How accurately can we date the duration of hydrothermal intrusive events in porphyry systems? *Economic Geology*, v. 108, p. 565–584

Claiborne, L. L., Miller, C. F., Flanagan, D. M., Clyne, M. A., and Wooden, J. L., 2010, Zircon reveals protracted magma storage and recycling beneath Mount St. Helens: *Geology*, v. 38, p. 1011–1014.

Cline, J. S., and Bodnar, R. J., 1991, Can economic porphyry copper mineralization be generated by a typical calc-alkaline melt? *Journal of Geophysical Research: Solid Earth*, v. 96, p. 8113–8126.

Cloos, M., Sapiie, B., van Ufford, A. Q., Weiland, R. J., Warren, P. Q., and McMahon, T. P., 2005, Collisional delamination in New Guinea: The geotectonics of subducting slab breakoff: *Geological Society of America Special Papers*, v. 400, p. 1–51.

Condon, D., Schoene, B., McLean, N., Bowring, S., and Parrish, R., 2015, Metrology and traceability of U–Pb isotope dilution geochronology (EARTHTIME Tracer Calibration Part I): *Geochimica et Cosmochimica Acta*, v. 164, p. 464–480.

Cooke, D. R., Hollings, P., and Walshe, J. L., 2005, Giant porphyry deposits: characteristics, distribution, and tectonic controls: *Economic Geology*, v. 100, p. 801–818.

Crowley, J., Schoene, B., and Bowring, S., 2007, U-Pb dating of zircon in the Bishop Tuff at the millennial scale: *Geology*, v. 35, p. 1123–1126.

Davies, H., Howell, W., Fardon, R., Carter, R., and Bumstead, E., 1978, History of the Ok Tedi porphyry copper prospect, Papua New Guinea; I, The years 1966 to 1976; II, The years 1975 to 1978: *Economic Geology*, v. 73, p. 796–809.

Davies, H. L., 2012, The geology of New Guinea - the cordilleran margin of the Australian continent: *Episodes*, v. 35, p. 87–102.

Dilles, J. H., 1987, Petrology of the Yerington Batholith, Nevada; evidence for evolution of porphyry copper ore fluids: *Economic Geology*, v. 82, p. 1750–1789.

Dilles, J. H., Kent, A. J., Wooden, J. L., Tosdal, R. M., Koleszar, A., Lee, R. G., and Farmer, L. P., 2015, Zircon compositional evidence for sulfur-degassing from ore-forming arc magmas: *Economic Geology*, v. 110, p. 241–251.

Doucette, J., 2000, A petrochemical study of the Mount Fubilan Intrusion and associated ore bodies, Papua New Guinea: Unpublished Ph.D. thesis, Corvallis, Oregon State University, 373 p.

Ferry, J., and Watson, E., 2007, New thermodynamic models and revised calibrations for the Ti-in-zircon and Zr-in-rutile thermometers: *Contributions to Mineralogy and Petrology*, v. 154, p. 429–437.

Gaina, C., Müller, R. D., Brown, B., Ishihara, T., and Ivanov, S., 2007, Breakup and early seafloor spreading between India and Antarctica: *Geophysical Journal International*, v. 170, p. 151–169.

Gerstenberger, H., and Haase, G., 1997, A highly effective emitter substance for mass spectrometric Pb isotope ratio determinations: *Chemical Geology*, v. 136, p. 309–312.

Gustafson, L. B., and Hunt, J. P., 1975, The porphyry copper deposit at El Salvador, Chile: *Economic Geology*, v. 70, p. 857–912.

Halter, W. E., Heinrich, C. A., and Pettke, T., 2005, Magma evolution and the formation of porphyry Cu–Au ore fluids: evidence from silicate and sulfide melt inclusions: *Mineralium Deposita*, v. 39, p. 845–863.

Hattori, K. H., and Keith, J. D., 2001, Contribution of mafic melt to porphyry copper mineralization: evidence from Mount Pinatubo, Philippines, and Bingham Canyon, Utah, USA: *Mineralium Deposita*, v. 36, p. 799–806.

Hiess, J., Condon, D. J., McLean, N., and Noble, S. R., 2012, $^{238}\text{U}/^{235}\text{U}$ systematics in terrestrial uranium-bearing minerals: *Science*, v. 335, p. 1610–1614.

Hill, K. C., and Hall, R., 2003, Mesozoic-Cenozoic evolution of Australia's New Guinea margin in a west Pacific context: *Geological Society of America Special Papers*, v. 372, p. 265–290.

Holm, R. J., 2013, Magmatic arcs of Papua New Guinea: insights into the late Cenozoic tectonic evolution of the northern Australian plate boundary: Doctoral dissertation, Townsville, Australia, James Cook University, p. 221.

Holm, R. J., Spandler, C., and Richards, S. W., 2015, Continental collision, orogenesis and arc magmatism of the Miocene Maramuni arc, Papua New Guinea: *Gondwana Research*, v. 28, p. 1117–1136.

Hoskin, P. W., 2005, Trace-element composition of hydrothermal zircon and the alteration of Hadean zircon from the Jack Hills, Australia: *Geochimica et Cosmochimica Acta*, v. 69, p. 637–648.

Huber, C., Bachmann, O., and Manga, M., 2009, Homogenization processes in silicic magma chambers by stirring and mushification (latent heat buffering): *Earth and Planetary Science Letters*, v. 283, p. 38–47.

Jackson, S. E., Pearson, N. J., Griffin, W. L., and Belousova, E. A., 2004, The application of laser ablation-inductively coupled plasma-mass spectrometry to in situ U–Pb zircon geochronology: *Chemical Geology*, v. 211, p. 47–69.

Jaffey, A., Flynn, K., Glendenin, L., Bentley, W. t., and Essling, A., 1971, Precision measurement of half-lives and specific activities of ^{235}U and ^{238}U : *Physical Review C*, v. 4, p. 1889.

Johnson, R., and Jaques, A., 1980, Continent—arc collision and reversal of arc polarity: New interpretations from a critical area: *Tectonophysics*, v. 63, p. 111–124.

Johnson, R., Mackenzie, D., and Smith, I., 1978, Delayed partial melting of subduction-modified mantle in Papua New Guinea: *Tectonophysics*, v. 46, p. 197–216.

Johnson, T., and Molnar, P., 1972, Focal mechanisms and plate tectonics of the southwest Pacific: *Journal of Geophysical Research*, v. 77, p. 5000–5032.

Krogh, T., 1973, A low-contamination method for hydrothermal decomposition of zircon and extraction of U and Pb for isotopic age determinations: *Geochimica et Cosmochimica Acta*, v. 37, p. 485–494.

Kueter, N., Soesilo, J., Fedortchouk, Y., Nestola, F., Belluco, L., Troch, J., Wälle, M., Guillong, M., Von Quadt, A., and Driesner, T., 2016, Tracing the depositional history of Kalimantan diamonds by zircon provenance and diamond morphology studies: *Lithos*, v. 265, p. 159–176.

Landtwing, M. R., Dillenbeck, E. D., Leake, M. H., and Heinrich, C. A., 2002, Evolution of the breccia-hosted porphyry Cu-Mo-Au deposit at Agua Rica, Argentina: progressive unroofing of a magmatic hydrothermal system: *Economic Geology*, v. 97, p. 1273–1292.

Lee, R. G., Dilles, J. H., Tosdal, R. M., Wooden, J. L., and Mazdab, F. K., 2017, Magmatic Evolution of Granodiorite Intrusions at the El Salvador Porphyry Copper Deposit, Chile, Based on Trace Element Composition and U/Pb Age of Zircons: *Economic Geology*, v. 112, p. 245–273.

Loader, M. A., Wilkinson, J. J., and Armstrong, R. N., 2017, The effect of titanite crystallisation on Eu and Ce anomalies in zircon and its implications for the assessment of porphyry Cu deposit fertility: *Earth and Planetary Science Letters*, v. 472, p. 107–119.

Longo, A. A., Dilles, J. H., Grunder, A. L., and Duncan, R., 2010, Evolution of calc-alkaline volcanism and associated hydrothermal gold deposits at Yanacocha, Peru: *Economic Geology*, v. 105, p. 1191–1241.

Mason, R., 1997, Structure of the Alice anticline, Papua New Guinea: serial balanced cross-sections and their restoration: *Journal of Structural Geology*, v. 19, p. 719–734.

Mattinson, J. M., 2005, Zircon U–Pb chemical abrasion (“CA-TIMS”) method: combined annealing and multi-step partial dissolution analysis for improved precision and accuracy of zircon ages: *Chemical Geology*, v. 220, p. 47–66.

McLean, N. M., Bowring, J., and Bowring, S., 2011, An algorithm for U-Pb isotope dilution data reduction and uncertainty propagation: *Geochemistry, Geophysics, Geosystems*, v. 12, p. 1–26.

McLean, N. M., Condon, D. J., Schoene, B., and Bowring, S. A., 2015, Evaluating uncertainties in the calibration of isotopic reference materials and multi-element isotopic tracers (EARTHTIME Tracer Calibration Part II): *Geochimica et Cosmochimica Acta*, v. 164, p. 481–501.

McNaughton, N. J., Mueller, A. G., and Groves, D. I., 2005, The age of the giant Golden Mile deposit, Kalgoorlie, Western Australia: Ion-microprobe zircon and monazite U-Pb geochronology of a synmineralization lamprophyre dike: *Economic Geology*, v. 100, p. 1427–1440.

Mercer, C. N., Reed, M. H., and Mercer, C. M., 2015, Time scales of porphyry Cu deposit formation: insights from titanium diffusion in quartz: *Economic Geology*, v. 110, p. 587–602.

Miller, J. S., Matzel, J. E., Miller, C. F., Burgess, S. D., and Miller, R. B., 2007, Zircon growth and recycling during the assembly of large, composite arc plutons: *Journal of Volcanology and Geothermal Research*, v. 167, p. 282–299.

Ok Tedi Mining Limited, 2017, Annual Review (<http://www.oktedi.com/media-items/publications/annual-review/488-2016-annual-review/file>).

Page, R., 1975, Geochronology of late Tertiary and Quaternary mineralized intrusive porphyries in the Star Mountains of Papua New Guinea and Irian Jaya: *Economic Geology*, v. 70, p. 928–936.

Page, R., and McDougall, I., 1972, Ages of mineralization of gold and porphyry copper deposits in the New Guinea Highlands: *Economic Geology*, v. 67, p. 1034–1048.

Parmigiani, A., Faroughi, S., Huber, C., Bachmann, O., and Su, Y., 2016, Bubble accumulation and its role in the evolution of magma reservoirs in the upper crust: *Nature*, v. 532, p. 492–507.

Paton, C., Hellstrom, J., Paul, B., Woodhead, J., and Hergt, J., 2011, Iolite: Freeware for the visualisation and processing of mass spectrometric data: *Journal of Analytical Atomic Spectrometry*, v. 26, p. 2508–2518.

Petrus, J. A., and Kamber, B. S., 2012, VizualAge: A Novel Approach to Laser Ablation ICP-MS U-Pb Geochronology Data Reduction: *Geostandards and Geoanalytical Research*, v. 36, p. 247–270.

Pigram, C., Davies, P., Feary, D., and Symonds, P., 1989, Tectonic controls on carbonate platform evolution in southern Papua New Guinea: passive margin to foreland basin: *Geology*, v. 17, p. 199–202.

Pollard, P. J., 2014, Grade distribution of the giant Ok Tedi Cu-Au deposit, Papua New Guinea—a discussion: *Economic Geology*, v. 109, p. 1489–1492.

Pollard, P. J., Taylor, R. G., and Peters, L., 2005, Ages of intrusion, alteration, and mineralization at the Grasberg Cu-Au deposit, Papua, Indonesia: *Economic Geology*, v. 100, p. 1005–1020.

Pollard, P. J., Smilie, R. W., Stein, H. J., and Hastings, D. R., 2015, High-precision Re-Os molybdenite ages for porphyry- and skarn-style Cu-Au mineralization at Ok Tedi, Papua New Guinea: SEG conferece 2015, Hobart; Abstract Volume.

Proffett, J. M., 2003, Geology of the Bajo de la Alumbrera porphyry copper-gold deposit, Argentina: *Economic Geology*, v. 98, p. 1535–1574.

Redmond, P. B., and Einaudi, M. T., 2010, The Bingham Canyon porphyry Cu-Mo-Au deposit. I. Sequence of intrusions, vein formation, and sulfide deposition: *Economic Geology*, v. 105, p. 43–68.

Reid, M. R., Vazquez, J. A., and Schmitt, A. K., 2011, Zircon-scale insights into the history of a Supervolcano, Bishop Tuff, Long Valley, California, with implications for the Ti-in-zircon geothermometer: *Contributions to Mineralogy and Petrology*, v. 161, p. 293–311.

Rezeau, H., Moritz, R., Wotzlaw, J. F., Ovtcharova, M., Tayan, R., Melkonyan, R., Hovakimyan, S., Ramayanov, V., Selby, D., Ulianov, A., Chiaradia, M., and Putliz, B., 2016, Temporal and genetic link between incremental pluton assembly and pulsed porphyry Cu-Mo formation in accretionary orogens: *Geology*, v. 44, p. 627–630.

Richards, J. P., Chappell, B. W., and McCulloch, M. T., 1990, Intraplate-type magmatism in a continent-island-arc collision zone: Porgera intrusive complex, Papua New Guinea: *Geology*, v. 18, p. 958–961.

Rohrlach, B. D., Loucks, R. R., and Porter, T. M., 2005, Multi-million-year cyclic ramp-up of volatiles in a lower crustal magma reservoir trapped below the Tampakan copper-gold deposit by Mio-Pliocene crustal compression in the southern Philippines, in Porter T. M., ed., *Super Porphyry Copper and Gold*

Deposits — A Global Perspective, 2nd edition, Adelaide, PCG Publishing, p. 369–407.

Rubatto, D., and Hermann, J., 2007, Experimental zircon/melt and zircon/garnet trace element partitioning and implications for the geochronology of crustal rocks: *Chemical Geology*, v. 241, p. 38–61.

Rush, P., and Seegers, H., 1990, Ok Tedi copper-gold deposits: *Geology of the mineral deposits of Australia and Papua New Guinea*, v. 2, p. 1747–1754.

Samperton, K. M., Schoene, B., Cottle, J. M., Keller, C. B., Crowley, J. L., and Schmitz, M. D., 2015, Magma emplacement, differentiation and cooling in the middle crust: Integrated zircon geochronological–geochemical constraints from the Bergell Intrusion, Central Alps: *Chemical Geology*, v. 417, p. 322–340.

Sasso, A. M., 1998, The Farallón Negro Group, northwest Argentina: magmatic, hydrothermal and tectonic evolution and implications for Cu-Au metallogeny in the Andean back-arc: *Society of Economic Geology Newsletter*, v. 34, p. 8–18.

Schaltegger, U., 2007, Hydrothermal zircon: *Elements*, v. 3, p. 51–79.

Schaltegger, U., Brack, P., Ovtcharova, M., Peytcheva, I., Schoene, B., Stracke, A., ... and Bargossi, G. M., 2009, Zircon and titanite recording 1.5 million years of magma accretion, crystallization and initial cooling in a composite pluton (southern Adamello batholith, northern Italy): *Earth and Planetary Science Letters*, v. 286, p. 208–218.

Schärer, U., 1984, The effect of initial ²³⁰Th disequilibrium on young UPb ages: the Makalu case, Himalaya: *Earth and Planetary Science Letters*, v. 67, p. 191–204.

Scherer, E., Münker, C., and Mezger, K., 2001, Calibration of the lutetium-hafnium clock: *Science*, v. 293, p. 683–687.

Schoene, B., Schaltegger, U., Brack, P., Latkoczy, C., Stracke, A., and Günther, D., 2012, Rates of magma differentiation and emplacement in a ballooning pluton recorded by U–Pb TIMS-TEA, Adamello batholith, Italy: *Earth and Planetary Science Letters*, v. 355, p. 162–173.

Seedorff, E., and Einaudi, M. T., 2004, Henderson porphyry molybdenum system, Colorado: I. Sequence and abundance of hydrothermal mineral assemblages, flow paths of evolving fluids, and evolutionary style: *Economic Geology*, v. 99, p. 3–37.

Sillitoe, R. H., 1985, Ore-related breccias in volcanoplutonic arcs: *Economic Geology*, v. 80, p. 1467–1514.

Sillitoe, R. H., 1997, Characteristics and controls of the largest porphyry copper-gold and epithermal gold deposits in the circum-Pacific region: *Australian Journal of Earth Sciences*, v. 44, p. 373–388.

Sillitoe, R. H., 2010, Porphyry copper systems: *Economic Geology*, v. 105, p. 3–41.

Sillitoe, R. H., and Perelló, J., 2005, Andean copper province: Tectonomagmatic settings, deposit types, metallogeny, exploration, and discovery: *Economic Geology*, 100th Anniversary Volume, p. 845–890.

Steinberger, I., Hinks, D., Driesner, T., and Heinrich, C. A., 2013, Source plutons driving porphyry copper ore formation: combining geomagnetic data, thermal constraints, and chemical mass balance to quantify the magma chamber beneath the Bingham Canyon deposit: *Economic Geology*, v. 108, p. 605–624.

Tapster, S., Condon, D., Naden, J., Noble, S., Petterson, M., Roberts, N., Saunders, A., and Smith, D., 2016, Rapid thermal rejuvenation of high-crystallinity magma linked to porphyry copper deposit formation; evidence from the Koloula Porphyry Prospect, Solomon Islands: *Earth and Planetary Science Letters*, v. 442, p. 206–217.

Tregoning, P., and Gorbatov, A., 2004, Evidence for active subduction at the New Guinea Trench: *Geophysical Research Letters*, v. 31, p. 1–4.

Van Dongen, M., Weinberg, R., Tomkins, A., Armstrong, R., and Woodhead, J., 2010a, Recycling of Proterozoic crust in Pleistocene juvenile magma and rapid formation of the Ok Tedi porphyry Cu–Au deposit, Papua New Guinea: *Lithos*, v. 114, p. 282–292.

Van Dongen, M., Weinberg, R. F., and Tomkins, A. G., 2010b, REE-Y, TI, and P remobilization in magmatic rocks by hydrothermal alteration during Cu-Au deposit formation: *Economic Geology*, v. 105, p. 763–776.

Van Dongen, M., Weinberg, R. F., and Tomkins, A. G., 2013, Grade distribution of the giant OK Tedi Cu-Au deposit, Papua New Guinea: *Economic Geology*, v. 108, p. 1773–1781.

Vervoort, J. D., and Blichert-Toft, J., 1999, Evolution of the depleted mantle: Hf isotope evidence from juvenile rocks through time: *Geochimica et Cosmochimica Acta*, v. 63, p. 533–556.

Von Quadt, A., Erni, M., Martinek, K., Moll, M., Peytcheva, I., and Heinrich, C. A., 2011, Zircon crystallization and the lifetimes of ore-forming hydrothermal intrusive systems: *Geology*, v. 39, p. 731–734.

Von Quadt, A., Wotzlaw, J.-F., Buret, Y., Large, S. J., Peytcheva, I., and Trinquier, A., 2016, High-precision zircon U/Pb geochronology by ID-TIMS using new 10 13 ohm resistors: *Journal of Analytical Atomic Spectrometry*, v. 31, p. 658–665.

Watson, E., and Harrison, T., 2005, Zircon thermometer reveals minimum melting conditions on earliest Earth: *Science*, v. 308, p. 841–844.

Watson, E. B., Wark, D. A., and Thomas, J. B., 2006, Crystallization thermometers for zircon and rutile: *Contributions to Mineralogy and Petrology*, v. 151, p. 413–433.

Weis, P., Driesner, T., and Heinrich, C., 2012, Porphyry-copper ore shells form at stable pressure-temperature fronts within dynamic fluid plumes: *Science*, v. 338, p. 1613–1616.

Wiedenbeck, M., Alle, P., Corfu, F., Griffin, W., Meier, M., Oberli, F., Quadt, A. v., Roddick, J., and Spiegel, W., 1995, Three natural zircon standards for U-Th-Pb, Lu-Hf, trace element and REE analyses: *Geostandards newsletter*, v. 19, p. 1–23.

Wilkinson, J. J., 2013, Triggers for the formation of porphyry ore deposits in magmatic arcs: *Nature Geoscience*, v. 6, p. 917–925.

Wotzlaw, J.-F., Schaltegger, U., Frick, D. A., Dungan, M. A., Gerdes, A., and Günther, D., 2013, Tracking the evolution of large-volume silicic magma reservoirs from assembly to supereruption: *Geology*, v. 41, p. 867–870.

Wotzlaw, J.-F., Hüsing, S.K., Hilgen, F.J., and Schaltegger, U., 2014, High-precision zircon U-Pb geochronology of astromically dated volcanic ash beds from the Mediterranean Miocene: *Earth and Planetary Science Letters*, v. 407, p. 19–34.

Wotzlaw, J. F., Buret, Y., Large, S. J., Szymanowski, D., and von Quadt, A., 2017, ID-TIMS U–Pb geochronology at the 0.1‰ level using 10¹³ Ω resistors and simultaneous U and ¹⁸O/¹⁶O isotope ratio determination for accurate UO₂

interference correction: *Journal of Analytical Atomic Spectrometry*, v. 32, p. 579–586.